Uncertainty quantification in multiscale simulation of woven fiber composites

Ramin Bostanabad[a,1], Biao Liang[a,1], Jiaying Gao[a], Wing Kam Liu[a], Jian Cao[a],
Danielle Zeng[b], Xuming Su[b], Hongyi Xu[b], Yang Li[b], Wei Chen[a,*]

[a] *Department of Mechanical Engineering, Northwestern University, Evanston, IL 60208, United States*
[b] *Research & Advanced Engineering, Ford Motor Company, Dearborn, MI, 48121, United States*

Abstract

Woven fiber composites have been increasingly employed as light-weight materials in aerospace, construction, and transportation industries due to their superior properties. These materials possess a hierarchical structure that necessitates the use of multiscale simulations in their modeling. To account for the inherent uncertainty in materials, such simulations must be integrated with statistical uncertainty quantification (UQ) and propagation (UP) methods. However, limited advancement has been made in this regard due to the significant computational costs and complexities in modeling spatially correlated structural variations coupled at different scales. In this work, a non-intrusive approach is proposed for multiscale UQ and UP to address these limitations. We introduce the top-down sampling method that allows to model non-stationary and continuous (but not differentiable) spatial variations of uncertainty sources by creating nested random fields (RFs) where the hyperparameters of an ensemble of RFs is characterized by yet another RF. We employ multi-response Gaussian RFs in top-down sampling and leverage statistical techniques (such as metamodeling and dimensionality reduction) to address the considerable computational costs of multiscale simulations. We apply our approach to quantify the uncertainty in a cured woven composite due to spatial variations of yarn angle, fiber volume fraction, and fiber misalignment angle. Our results indicate that, even in linear analysis, the effect of uncertainty sources on the material's response could be significant.
© 2018 Elsevier B.V. All rights reserved.

1. Introduction

It is widely accepted that materials are heterogeneous and possess a hierarchical structure where the coarse-scale behavior is greatly affected by the fine-scale details (i.e., the microstructure). Because the traditional one-scale continuum mechanics does not suffice to investigate the effect of microstructure on materials' properties,

---

* Corresponding author.
  E-mail address: weichen@northwestern.edu (W. Chen).
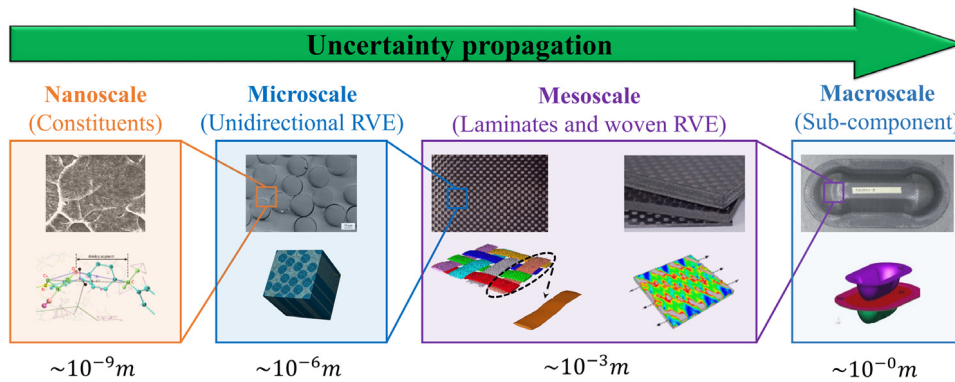[1] Equal contribution.

Fig. 1. (Color online) Schematic view of a four-scale woven fiber composite with polymer matrix: In computational modeling of this structure, each integration point at any scale is a realization of a structure at a finer scale. Due to the delicacy of materials at fine-scales, RVEs at lower scales may embody more uncertainty than those at higher scales. To quantify the uncertainty in a macroscopic quantity of interest, the relevant uncertainty sources at the lower scales should be identified for uncertainty propagation.

significant effort has been devoted to the development of multiscale computational models. These models have provided the means to study the effect of microstructure on many phenomena including damage evolution [1,2], fracture initiation [3], and strain localization [4].

Uncertainty is inevitably introduced in materials' behavior starting from the design and constituent selection stages, through the manufacturing processes, and finally during operation. For this reason, ever-growing research [5–7] is being conducted to rigorously couple computational models with statistical uncertainty quantification (UQ) and propagation (UP) methods to provide probabilistic predictions that are in line with the observed stochasticity in materials.

UQ and UP are actively pursued in various fields of science and engineering [6,8–23]. They are, however, seldom applied to multiscale simulations due to the significant computational costs and complexities. Our goal is to devise a non-intrusive UQ and UP approach that characterizes the uncertainties via random fields (RFs) and is applicable to multiscale simulations where multiple uncertainty sources (including spatial microstructural variations) arise from different length-scales. We are particularly interested in a non-intrusive approach because not only they are more general, but also *opening* multiscale computer models (i.e., changing the formulations) to directly introduce uncertainty sources into them requires considerable effort.

We take woven fiber composites as our motivating example. Such materials have been increasingly used in aerospace, construction, and transportation industries due to their superior properties including high strength-to-weight ratio, non-corrosive behavior [24], enhanced dimensional stability [25], and high impact resistance [26]. Woven fiber composites possess, as illustrated in Fig. 1, a hierarchical structure that spans multiple length-scales. *Macroscale* is at the highest length-scale where the overall mechanical performance under some loading conditions is evaluated and characteristics such as fiber and yarn (aka tow or bundle) volume fractions, effective properties, and part geometry are of interest. The individual yarns and their architecture (i.e., their dimension and relative spatial arrangement, see Fig. 2(a) and (b)) in the laminates are modeled in the *mesoscale*. The fibers (and their relative position within the yarns) and the matrix belong to the *microscale*. Finally, the constituent properties and the interaction between them (e.g., the interphase) are modeled in the *nanoscale*.

Multiple uncertainty sources that must be considered in the computational models are introduced at each of these length-scales [24]. For instance, during the preforming process, the high pressure and flow of the resin or draping change the *local architecture* of the fibers [27], see Fig. 2(c). Additionally, processing variations and material imperfections cause the *fiber volume fraction* to spatially vary over the part; especially along the yarn path where there is compact contact [28,29]. These macroscopic uncertainties are manifestations of a multitude of uncertainty sources that exist at the finer scales where, due to the delicacy of materials, the number and dimensionality of the uncertainty sources increase [10]. Moving down the scale ladder in Fig. 1, one can observe that the uncertainty sources are of different nature (e.g., morphological, geometrical, or property related), and spatially (within and across scales) correlated. These features render the UQ of a macroscopic quantity of interest extremely challenging. It is
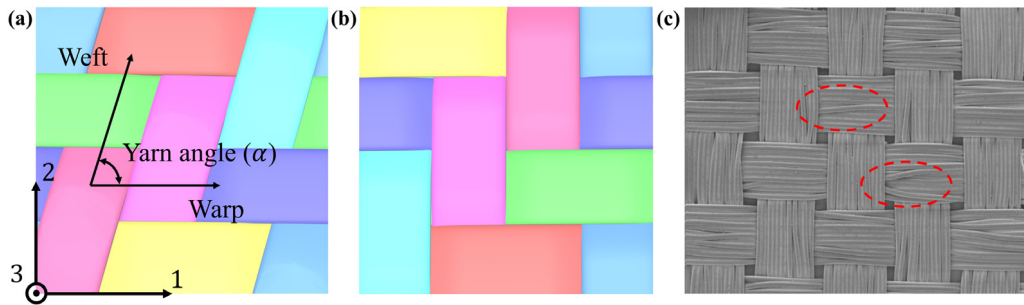
Fig. 2. (Color online) Some possible yarn architectures at the mesoscale for cured woven composites: Computational samples of 2×2 (a) non-orthogonal and (b) orthogonal woven fabrics with side measures of 4 yarns in-plane (generated with *TexGen* [30]). (c) Illustration of fiber misalignment in woven composites [31]. In these images, the resin is not shown to better demonstrate the yarns.

further noted that macroscopic uncertainty depends heavily on the quantity of interest. For example, the homogenized response in linear analyses and damage are clearly not equally sensitive to spatial microstructural variations.

To illustrate the various uncertainty sources along with the abovementioned challenges associated with UQ and UP tasks in multiscale materials we narrow our focus, as depicted in Fig. 3, to two scales from the composite in Fig. 1. In the finite element (FE) mesh of the mesostructure in Fig. 3, there are over 10 000 integration points (IP's, aka Gauss or material points). Each of these points can be thought of as a realization of a sufficiently large structure (aka representative volume element, RVE) at the next finer scale, i.e., the microscale. A widely-recognized method for modeling the behavior of such a hierarchical material is through *computational homogenization*. This method involves the solution of partial differential equations (PDEs) at both scales where the boundary conditions of the microscale PDEs are determined at the mesoscale. Once the microscale PDEs are solved, the homogenized stresses and tangent moduli are passed up to be used in the PDEs at the mesoscale. If the FE method is used in both scales to solve the boundary value problems, this method is referred to as FE^2 [32,33]. Since the FE^2 method is generally very expensive, many recent works have focused on more efficient methods [34–37].
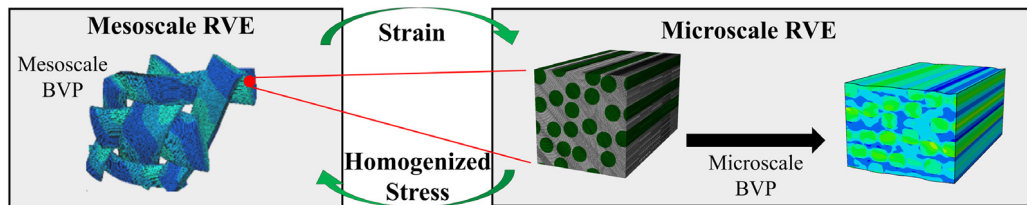

Fig. 3. (Color online) Computational homogenization in a two-scale structure: The boundary values (i.e., the applied strains) at the microscale are passed down from the mesoscale to the microstructure. Once the boundary value problem (BVP) is solved at the microscale (i.e., the microstructure is deformed to conform to the applied strain), the homogenized stresses and tangent moduli are passed up to be used in the mesoscale BVP. The resin is hidden in the mesostructure for a better illustration.

In a deterministic simulation, all the parameters (and their evolution) at the IPs in both scales (related to, e.g., the material properties, the morphology, or the applied load) are known *a priori*. In the presence of uncertainty, however, such parameters may only be characterized statistically. For instance, in the mesoscopic RVE in Fig. 3, the dimensions and relative arrangement of the yarns, the fiber volume fraction, and material properties (such as Young's modulus and Poisson ratio) might vary *spatially* due to multiple factors such as manufacturing inconsistencies. These spatial variations across the IPs of the mesostructure imply that the corresponding microstructures are not identical. More importantly, these mesoscale variations are spatially correlated. For instance, the data reported in [27,28,38] demonstrate that in unidirectionally reinforced fiber composites (with either metallic or polymeric matrix) not only the fiber misalignment angles and volume fraction change spatially, but also these changes are negatively correlated (i.e., high volume fraction implies small misalignment angle and vice versa). Similarly, some of the properties and parameters at the microstructures might be spatially inhomogeneous. Hence, to quantify the mesoscale uncertainty, the microscale stochasticity must be *quantified*, *propagated*, and finally *coupled* with uncertainty sources at the mesoscale.

One way to quantify the uncertainty of an effective coarse-scale property (e.g., shear or Young's moduli), is via Monte Carlo (MC) sampling where many simulations are conducted to find the distributional characteristics. However,

MC sampling is practically infeasible in multiscale simulations due to (i) the curse of dimensionality that arises from the number of IPs (i.e., degrees of freedom), (ii) the nested nature of the uncertainty sources, and (iii) the high cost of multiscale simulations. For example, in the two-scale structure in Fig. 3, a *single* MC sample would consist of:

1. Assigning correlated parameters (morphological, geometrical, property related, and so on) to all the IPs of the mesostructure.
2. Generating microstructures where each one is consistent with the assigned parameters to the corresponding IP in the mesoscale.
3. Conducting a multiscale simulation via, e.g., the FE^2 method.

As the number of scales and uncertainty sources increase (see Fig. 1), the computational costs of UQ and UP analyses rapidly increase. More efficient sampling techniques (such as quasi MC, importance sampling, subset simulation, line sampling, and variants of Latin hypercube sampling [39–41]) suffer from the same issue. Since the use of multiscale materials in science and engineering is rapidly growing, there is a clear need [6,42] for efficient methods and frameworks to quantify the coarse-scale uncertainty of such materials as a function of the fine-scale uncertainties. We believe that our approach paves the path to this end by leveraging the physics of the problem at hand in addition to the statistical UQ and UP methods. With our approach, fewer simulations could be used to determine the distributional characteristics.

There has been some work focused on UQ and UP in fibrous composites. Komeili and Milani [24] conducted a two-level factorial design at the mesoscale to illustrate the sensitivity of orthogonal woven fabrics to the yarn geometry (including yarn spacing, width, and height) and material properties. They concluded that, based on the applied load, these parameters could have a significant effect on the effective response (which was taken as the reaction force). A similar sensitivity study based on Sobol's indices was conducted in [12] to demonstrate that the friction coefficient and yarn height significantly affect the macroscale mechanical response of interest in dry woven fabrics. In [12,24], yarn properties do not spatially vary and fibers are well aligned. Savvas et al. [43,44] studied the required RVE size as a function of spatial variations of volume fraction and fiber architecture. They concluded that the RVE size must increase at higher volume fractions and, additionally, fiber orientation is more important than waviness in determining the mesoscale RVE size. In another work [17] they also illustrated that geometrical characteristics (i.e., the shape and arrangement of the fibers) and the material properties (Young's moduli of the constituents) affect the homogenized response (average axial and shear stiffness) in unidirectional (UD) composites quite significantly (with the former being more important). The variations were shown to decrease as the number of fibers and RVE size increased. Vanaerschot et al. [27] also studied the variability in composite materials' properties and concluded that the stiffness in the mesoscale RVE is affected by the load orientation [38] and, additionally, it significantly decreases as the fiber misalignment (see Fig. 2(c)) increases. In a series of works, Hsiao and Daniel [45–47] experimentally and theoretically investigated the effect of fiber waviness in UD composites. They demonstrated that under uniaxial compression loading the stiffness and strength decrease.

The focus of most prior works on UQ and UP in multiscale materials, as briefly reviewed above in the case of woven composites, has not been placed on rigorously modeling the uncertainty sources and statistically propagating their effects across multiple scales. For instance, modeling spatial variations via RFs, connecting them across different spatial scales, and investigating stochastic simulations are often neglected. On the contrary, as we review in Section 2, significant progress has been made in rigorous UQ and UP analyses in single-scale materials. Our goal is to exploit the strength of these two bodies of literature to devise a flexible approach for statistical uncertainty quantification and propagation in multiscale materials. To this end, we introduce the top-down sampling method that allows to model non-stationary and C^0 (i.e., continuous but not differentiable) RFs at fine length-scales (i.e., mesoscale and microscale) with a stationary and differentiable RF at the macroscale. We motivate the use of multi-response Gaussian processes to quantify the RFs and conduct sensitivity analyses for dimensionality reduction. The resulting approach is non-intrusive (in that the computational models need not be adapted to account for the uncertainties) and can leverage statistical techniques (such as metamodeling and dimensionality reduction) to address the considerable computational costs of multiscale simulations.

The rest of the paper is organized as follows. In Section 2, we review the methods and tools for single-scale UQ to motivate the need for quantifying the spatial variations via RFs. Our proposed approach is introduced in Section 3 which, in Section 4, is employed to quantify the macroscale uncertainty in a multiscale cured woven composite sample. We conclude the paper and provide future directions in Section 5.

2. Methodological base for uncertainty quantification and propagation

As opposed to multiscale materials such as fibrous composites, there are many works focused on UQ and UP in single-scale materials. Broadly speaking, there are three major methods for UQ and UP in computational mechanics' literature which use *MC sampling*, *the perturbation approach*, or *the spectral stochastic approach*. These three methods start with the random field representation of uncertainty sources. Next, the characterized field is discretized to assign random (but correlated) values to the finite elements. Finally, the simulations are done to study the response variability. Below, we elaborate on each of these procedures.

2.1. Random field representation of uncertainty sources

A random field (RF, aka stochastic process) is a collection of random variables (rv's) indexed in either time or space [48]. More formally, let us denote a probability space by $\{S, F, P\}$ where S is the sample space, F is the σ-algebra on S (i.e., it is a collection of subsets of S that also includes the empty subset), and P is the probability measure on F which specifies each event's likelihood of happening. Given the $\{S, F, P\}$ probability space, we define an RF as:

$$R(\boldsymbol{x}, s) \in \mathbb{R}^q, \boldsymbol{x} \in \mathbb{D} \subseteq \mathbb{R}^n, s \in S \tag{2.1}$$

where s is an outcome in S, and $\boldsymbol{x}$ is the n-dimensional field variable. Generally, $\boldsymbol{x}$ represents either space or time but it can also denote temperature field, stress or strain field, frequency, or a combination thereof. The domain of $\boldsymbol{x}$, $\mathbb{D}$, is either continuous or discrete. In practice, however, $\mathbb{D}$ is a finite set since even the continuous domains are discretized in computational environments. For example, in the context of computational mechanics, often $\boldsymbol{x}$ is taken to represent the spatial location of IPs or element centroids in a meshed structure. When $q = 1$, $R(\boldsymbol{x}, s)$ in Eq. (2.1) is a random variable for fixed $\boldsymbol{x} = \boldsymbol{x}_i$ and a function over all $\boldsymbol{x}$'s for a fixed outcome s_j. For $q > 1$, $R(\boldsymbol{x}_i, s_j)$ is a vector with q elements which might be correlated or not.[2]

The uncertainty sources in a material system might be mechanical (e.g., Young's modulus, Poisson ratio, yield stress, damage evolution parameters), geometrical (e.g., reinforcement distribution, fiber misalignment in composites), or operational (e.g., load variability). As these quantities change spatially (or temporally) within a material sample, RFs are generally employed to represent them. To illustrate how spatial variations can be modeled via RFs, we use the $1D$ bar in Fig. 4(a). In our pedagogical example, the goal is to assign the three parameters[3] $[v, \varphi, \theta]$ to the 20 IPs given the mean values over the entire bar, i.e., $[\overline{v}, \overline{\varphi}, \overline{\theta}] = [55, 0, 5]$. For this purpose, an RF with three responses ($q = 3$) could be employed for uncertainty quantification. Here, x would be the spatial location of each IP (measured, e.g., from one end of the bar), and the three outputs of the RF at each location x_i along the bar would correspond to the three parameters at that location, i.e., $[v_i, \varphi_i, \theta_i]$. Moreover, if it is believed that some of the outputs are independent, positively/negatively correlated (e.g., both v and φ increase/decrease along the bar), or change rapidly across the IPs, the RF should be able to capture that. In panels (b) through (c) in Fig. 4 four different scenarios are demonstrated. In panel (b), the RF's parameters are chosen to arrive at (i) spatially uncorrelated parameters (e.g., the change in v across the IPs is uncorrelated with that of θ), (ii) smooth transitions for each parameter across the IPs, and (iii) small changes for each parameter around the corresponding mean values. In panel (c), the changes are increased and so the realizations tend to deviate more from the mean values. In panel (d), a negative spatial correlation between v and the other two parameters is also added. This means that, *on average*, as v tends to increase along the IPs the other two parameters decrease and vice versa. Finally, in panel (e), the constraint on smooth transitions across the IPs is relaxed to allow the parameters to change rapidly from one IP to the next.

Although an RF is completely characterized by its nth order distribution function, this information is often too cumbersome to collect. Hence, RFs are generally defined by their mean and covariance functions. In computational mechanics' community, often the RFs are divided to two groups: Gaussian and non-Gaussian.

---

[2] s implies the random nature of the process and is generally dropped from the formulations.

[3] The reason behind our choice on the number and nature of these parameters will become clear in Section 4.1.
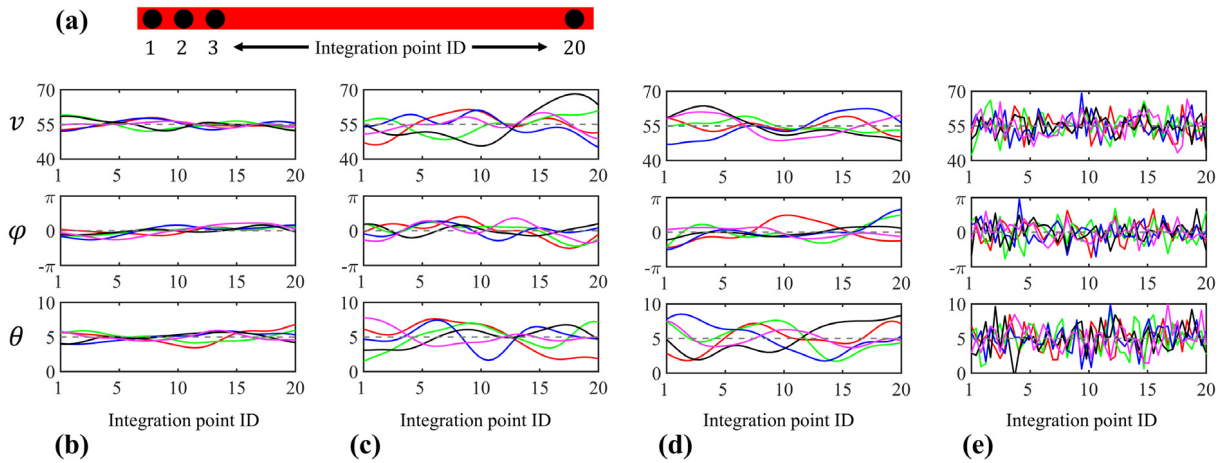
Fig. 4. (Color online) Pedagogical example on spatial variations: (a) A $1D$ bar which is discretized with 20 IPs. The spatial variations of the three parameters $[v, \varphi, \theta]$ across the IPs can take many forms, four of which are indicated in panels (b) through (e). The figures are all generated with the same RF but, from one panel to another, some of the RF's parameters are changed to achieve different spatial variations. In each panel, five realizations from the corresponding RF are drawn, and the prescribed mean value for each parameter is indicated with a dashed gray line. See the text for the detailed discussions on the differences across the four panels.

2.1.1. Simulations of Gaussian random fields

Gaussian random fields (GRFs) are ubiquitously employed in science and engineering due to their simplicity, tractability, and flexibility. These fields are completely characterized by their mean and covariance functions (i.e., 1st and 2nd moments) and naturally arise as a result of the central limit theorem. Moreover, often (esp. in materials science) there is scarce information on higher order moments and so GRFs are among the few available options for uncertainty quantification of spatially varying quantities.

Three main methods are generally used for the simulation of GRFs: the spectral representation method, Karhunen–Loève (KL) expansion, and the best linear unbiased predictor (BLUP). Below, we briefly describe the first two methods and, as we use the third method in our approach, elaborate on the BLUP approach in Section 4.3 and Appendix A.1.

With the spectral representation method, a GRF is expanded as a sum of trigonometric functions with random amplitudes and phase angles. In most applications, however, only the phase angles are assumed as random to sample functions that are ergodic in both the mean and auto-covariance [49]. With this assumption, based on the spectral density function $\rho(k)$ where k denotes the frequency, an analytical approach can be used to generate the realization $\hat{R}(x)$ from a GRF:

$$\hat{R}(x) = \left(\frac{2}{N}\right)^{1/2} \sum_{i=1}^{N} \cos(k_i \hat{k}_i \cdot x + \phi_i), \tag{2.2}$$

where ϕ_i is uniformly distributed on $[0, 2\pi]$, and $\hat{k}_i$ is uniformly distributed on a unit circle. k_i is a random variable whose probability density function, $P(k)$, is determined by the spectral density function: $P(k) = \rho(k)k$ and $P(k) = \rho(k)k^2$ for, respectively, two and three dimensional GRFs. Here, $\rho(k)$ must be determined by the user or calculated via some experimental data. This method of generating realizations of a GRF is also known as the Cahn's scheme and has been previously used to generate realizations of microstructures of random heterogeneous media [50–53].

Analogous to the Fourier series representation of functions, the KL expansion represents RFs as a summation of some weighted orthogonal functions. Unlike Fourier series, however, in the KL expansion the coefficients are random variables and the orthogonal bases depend on the decomposed RF. The KL expansion, also known as principal orthogonal decomposition, is closely related to principal component analysis (PCA) in that the orthogonal functions used in the expansion are the eigenfunctions of the RF's covariance function, c:

$$\hat{R}(x) = \overline{R}(x) + \sum_{i=1}^{\infty} \sqrt{\lambda_i} v_i(x) \xi_i, \tag{2.3}$$

where $\overline{R}(x)$ is the expected value (i.e., the mean) of the RF, λ_i and $v_i(x)$ are, respectively, the eigenvalues and eigenfunctions of c, and ξ_i's are uncorrelated random variables. The series in Eq. (2.3) is, in practice, truncated to only include the significant terms (i.e., terms with larger eigenvalues).

2.1.2. Simulation of non-Gaussian random fields

Several quantities exhibit non-Gaussian spatial (or temporal) changes and hence are better modeled with non-Gaussian RFs. Modeling via these fields, though providing more flexibility, is much more complicated than their Gaussian counterparts as they require higher-order joint multidimensional density functions. Below, we summarize some of these methods and refer the interested reader to the cited references for more details.

Due to lack of data as well as computational issues, a number of studies have used the *translation field* concept to generate a field through the non-linear transformation of an underlying GRF. Most of these methods, however, are iterative [54–56] and may not guarantee convergence because the marginal distribution of the RF (which is selected by the user) may not be compatible with the autocorrelation function of the translation field [57].

Copulas, which are multivariate distribution functions with marginal uniform distributions on the [0, 1] interval, provide another popular method for modeling non-Gaussian RFs. Uncertainty quantification with copulas has been previously used to analyze highly correlated random variables in finance [58–60], reliability-based design optimization [61], mechanics [10], and hydrology [62]. Following the above definition, an n-dimensional copula denoted by C_p is defined as:

$$F_{X_1, X_2, \ldots, X_n}(x_1, x_2, \ldots, x_n | \boldsymbol{P}) = C_p(F_{X_1}(x_1), F_{X_2}(x_2), \ldots, F_{X_n}(x_n) | \boldsymbol{P}'), \qquad (2.4)$$

where $F_{X_1, X_2, \ldots, X_n}(x_1, x_2, \ldots, x_n | \boldsymbol{P}) = F_X(\boldsymbol{x} | \boldsymbol{P})$ is the joint cumulative distribution function (CDF) of the multivariate random variable $\boldsymbol{X} = [X_1, X_2, \ldots, X_n]^T$ with correlation matrix $\boldsymbol{P}$, $F_{X_i}(x_i)$ is the marginal CDF of the random variable X_i, and $\boldsymbol{P}'$ is an invariant correlation matrix with entries in $[-1, 1]$ interval. We note that, herein we have adopted the statistical notation of representing random variables and their values (a real number) with, respectively, uncial and minuscule letters.

With the definition in Eq. (2.4), copula acts as a link that couples arbitrary marginal distributions to a joint distribution. To arrive at an alternate formulation, we note that the marginal CDF $F_{X_i}(x_i)$ is, by definition, a uniform rv on [0, 1]. That is:

$$F_{X_i}(x_i) = u_i \text{ and } u_i \in [0, 1]. \qquad (2.5)$$

Taking the inverse of Eq. (2.5) and replacing for x_i's and $F_{X_i}(x_i)$'s in Eq. (2.4), would represent C_p as a function that maps uniform rv's on $[0, 1]^n$ hypercube to some joint CDF which itself is represented as (inverse) marginal CDF's of those rv's:

$$F_X\left(F_{X_1}^{-1}(u_1), \ldots, F_{X_n}^{-1}(u_n) | \boldsymbol{P}\right) = C_p(u_1, u_2, \ldots, u_n | \boldsymbol{P}'). \qquad (2.6)$$

There are several types of copulas such as Gaussian copulas. Typically, the most cumbersome step in finding these copulas based on some datasets lies in building the transformed correlation matrix.

Polynomial chaos expansion (PCE) provides another flexible and widely popular method for uncertainty quantification of spatially varying quantities in a variety of applications including solid mechanics [10,11,63–65], computational fluid dynamics [66], and diffusion [67]. PCE decomposes a square-integrable rv or RF of unknown form to a series of orthogonal polynomial functions of some rv's (e.g., Gaussian, Poisson, or uniform). Following the notation of Eq. (2.1) and using Gaussian rv's for the expansion, we have:

$$\hat{R}(x) = a_0 \Gamma_0 + \sum_{i_1=1}^{\infty} a_{i_1} \Gamma_1(\xi_{i_1}) + \sum_{i_1}^{\infty} \sum_{i_2=1}^{i_1} a_{i_1 i_2} \Gamma_2(\xi_{i_1}, \xi_{i_2}) + \cdots, \qquad (2.7)$$

where $\{\xi_i(x)\}_{i=1}^{\infty}$ are independent and identically distributed (iid) standard normal rv's, Γ_k is the Wiener polynomial chaos of order k, and $a_{i_1 i_2 \ldots}$ are coefficients or functions in $\mathbb{D} \subseteq \mathbb{R}^n$. Having chosen normal rv's for the expansion (through ξ_i's), orthogonality of successive Γ_k requires them to be multivariate Hermit polynomials (which can be constructed via the tensor product of univariate Hermit polynomial). Eq. (2.7) converges, in a mean-square sense, to the random process $R(x)$ with the same marginal distributions. Due to limited data and computational reasons, however, the series is generally truncated.

2.2. Random field discretization

As briefly mentioned in Section 2.1, continuous or not, RFs are discretized in computational environments and hence represent the random quantities of the material as a vector of rv's. These rv's are then used in the FE mesh with either a *point-type method* or an *average-type method*. With the former approach, the rv's are simply assigned to some specific points in the FE mesh (e.g., IPs or element centroid). Representatives of this approach include midpoint, nodal point, integration point, and interpolation methods [68,69]. With the average-type method, however, the rv's are defined as some weighted integrals of the RF over each finite element. Local average and weighted integral methods [70,71] are examples of this approach.

The *stochastic mesh* [64], constructed by the spatial location of the rv's over the structure domain could be of different resolution than the FE mesh (i.e., finer, coarser, or the same). The advantage of using a coarse stochastic mesh lies in dimensionality reduction: as each rv counts as one dimension in the UQ and UP analyses, a coarse stochastic mesh would decrease the computational costs. In a fine mesh, however, the spatial correlations among the varying quantities (e.g., Young's modulus) are better captured and the parameter assignment is much easier. It is obvious that the optimal choice requires a compromise between cost, accuracy, and simplicity.

2.3. The stochastic finite element method

The stochastic finite element method (SFEM) is an extension of the ordinary case where the material characteristics or boundary conditions are, rather than deterministic, random. In SFEM, the formulation of the stochastic finite element matrices is perhaps the most important step. For example, if Young's modulus varies according to the zero-mean random field $R(x)$, the stochastic stiffness matrix of a finite element, k^e, would have the following form [64,72]:

$$k^e = \int_{V^e} B^{e^T} D_0^e B^e dV^e, \tag{2.8}$$

where B^e is the deterministic strain–displacement matrix, V^e is the volume of the element, and D_0 is the random stress–strain matrix of the material which depends on $R(x)$. Once k^e's are constructed, the global stiffness matrix can be built and subsequently used for solving the algebraic problem involving loads and displacements. Solving such an algebraic problem is computationally demanding and so tremendous effort has been placed on how to best integrate the RF representation of uncertainty sources (discussed in Section 2.1) with the finite element formulations. As our focus in this work is on uncertainty, we omit the details on the finite element but note that:

- Eq. (2.8) has been used for various finite elements in the past. See [70,73].
- In dynamic problems, the mass and damping matrices can be random as well. The formulations in such problems are more complicated and costly. See [74,75].

Ghanem and Spanos [63,72] extended deterministic finite element analysis to consider random material properties. In their work, the input uncertainty was quantified with the KL expansion of a GRF while the output uncertainty through the PCE expansion of the nodal displacements. Notable works have extended the PCE-based finite element analysis for a variety of applications [16,17,64–66]. These extensions, however, are applicable to linear systems and computationally (as well as theoretically) difficult for multiscale UQ and UP.

3. The proposed approach for multiscale UQ and UP

As illustrated in Fig. 5, our approach for multiscale UQ and UP has two main stages: Intra-scale uncertainty quantification and inter-scale uncertainty propagation. We start by identifying the uncertainty sources at each scale and modeling them via RFs where one RF is associated with *each* structure realization (see Section 3.2 for the details). We employ RFs with *sensible* (i.e., physically interpretable) parameters for three main reasons (i) to easily *couple* the uncertainty sources across the scales and enable their propagation from lower to higher scales, (ii) to connect the most important parameters of the RFs to the features of the material system and hence identify the dominant uncertainty sources in a *physically meaningful* way, and (iii) to allow for a *non-intrusive* UQ procedure by directly using the RFs' outputs in the multiscale FE simulations (instead of adapting the FE formulations for UQ and UP as in Section 2.3). For these reasons, we use the BLUP representation of *multi-response Gaussian processes* (MRGPs). We provide the
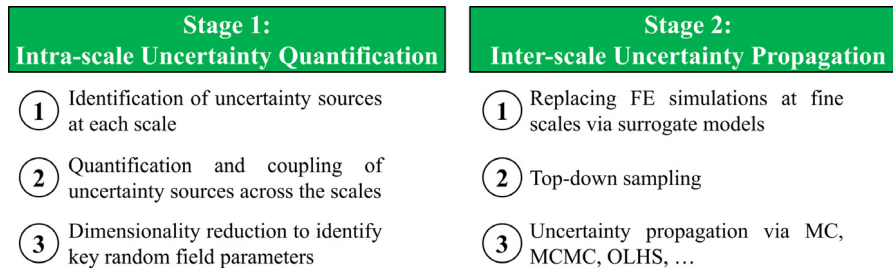
Stage 1: Intra-scale Uncertainty Quantification	Stage 2: Inter-scale Uncertainty Propagation
① Identification of uncertainty sources at each scale	① Replacing FE simulations at fine scales via surrogate models
② Quantification and coupling of uncertainty sources across the scales	② Top-down sampling
③ Dimensionality reduction to identify key random field parameters	③ Uncertainty propagation via MC, MCMC, OLHS, …

Fig. 5. Our approach for multiscale UQ and UP: The proposed approach has two main stages. In the first stage, the various uncertainty sources across different scales are identified and modeled with RFs. In the second stage, many realizations from the multiscale material are generated via the top-down sampling approach and, subsequently, simulated to propagate the uncertainty across the scales. To address the significant computational costs of multiscale simulations, dimension reduction and metamodeling techniques are employed in the first and second stages, respectively.

details on MRGPs in Section 3.1 but note here that they enable sensible characterization of uncertainty sources, are flexible and computationally efficient, and can be easily trained via available data [76].

At this point, the dimensionality in the UQ and UP tasks has been reduced from the number of degrees of freedom in the multiscale simulation to the few hyperparameters of the MRGP at the coarsest scale (see Sections 3.1 and 3.2 for the details). However, depending on the material system and quantities of interest, generally not all the hyperparameters need to be considered in the UP process. Hence, further *dimensionality reduction* can be achieved by identifying the dominant uncertainty sources and, equivalently, the corresponding RF parameters through, e.g., *sensitivity analysis* (SA).

The second stage of our approach starts by replacing the nested simulations at fine scales via inexpensive but accurate *metamodels* (aka surrogates or emulators) to decrease the computational costs of a single multi-scale simulation from hours (or even days) to minutes. The choice of the metamodel, its inputs, and its outputs depends on the nature of the finite element simulation (we elaborate on this with an example in Section 4.5). Finally, the uncertainty at the highest scale (e.g., macroscale in Fig. 1) is quantified by propagating the uncertainty from all the finer scales in the UP process. During UP, various multiscale simulations are conducted where in each simulation one realization of the spatially varying quantities are used in the multiscale material. To generate each of these realizations, we introduce the *top-down* sampling approach where realizations are assigned to the spatially varying parameters from the coarsest scale to the finest scale in the material system. We elaborate on the details in Section 4.3 but note that this sampling strategy enables modeling (*i*) non-stationary and C^0 (i.e., continuous but not differentiable) spatial variations at the fine-scales, and (*ii*) partial correlations between the various uncertainty sources within and across scales. Although the top-down sampling method can be integrated with any analytical RF, we have chosen MRGPs since they are sufficiently flexible and possess a few physically interpretable hyperparameters. Additionally, other RFs can sometimes be converted into GPs upon appropriate transformations.

More details on the proposed approach are provided below and in Section 4 where it is used to propagate the microscale and mesoscale uncertainties in a cured woven fiber composite to quantify the macroscale uncertainty.

3.1. Multi-response Gaussian processes for uncertainty quantification

MRGPs are widely popular in RF and surrogate modeling [76–83] and have been used in a wide range of applications including uncertainty quantification [77,81], machine learning [84], sensitivity analyses of complex computer models [85], Bayesian optimization [86], and tractable Bayesian calibration [87–91]. For an RF with q outputs $\mathbf{y} = [y_1, \ldots, y_q]^T$ and the field (e.g., spatial or temporal) inputs $\mathbf{x} = [x_1, \ldots, x_d]^T$, the BLUP representation of an MRGP with *constant* means reads as:

$$\mathbf{y} \sim \mathbb{N}_q \left(\boldsymbol{\beta}, c\left(\mathbf{x}, \mathbf{x}'\right) \right), \tag{3.1}$$

where $\mathbb{N}_q$ represents a q-dimensional Gaussian process, $\boldsymbol{\beta} = [\beta_1, \ldots, \beta_q]^T$ is the vector of responses' means, and $c\left(\mathbf{x}, \mathbf{x}'\right)$ is a parametric function that measures the covariance between the responses at $\mathbf{x}$ and $\mathbf{x}'$. One common choice

for $c\left(\boldsymbol{x}, \boldsymbol{x}'\right)$ is:

$$c\left(\boldsymbol{x}, \boldsymbol{x}'\right) = \boldsymbol{\Sigma} \bigotimes \exp\left\{\sum_{i=1}^{d} -10^{\omega_i}\left(x_i - x_i'\right)^2\right\} = \boldsymbol{\Sigma} \bigotimes r\left(\boldsymbol{x}, \boldsymbol{x}'\right), \qquad (3.2)$$

where $\boldsymbol{\Sigma}$ is a $q \times q$ symmetric positive definite matrix that captures the marginal variances and the covariances between the outputs, d is the dimensionality of the field, $\boldsymbol{\omega} = [\omega_1, \ldots, \omega_d]^T$ are the so-called roughness or scale parameters that control the smoothness of the RF, and $\bigotimes$ is the Kronecker product. Note that the dimension of $\boldsymbol{\beta}$ and $\boldsymbol{\Sigma}$ depends on q while that of $\boldsymbol{\omega}$ depends on d. The parameters $\boldsymbol{\beta}$, $\boldsymbol{\Sigma}$, and $\boldsymbol{\omega}$ are called the hyperparameters of an MRGP model and, collectively, enable it to model a wide range of random processes:

- The mean values of the responses over the entire input space are governed by $\boldsymbol{\beta}$.
- The general correlation between the responses (i.e., y_i and y_j, $i \neq j$) over the input space is captured by the off-diagonal elements of $\boldsymbol{\Sigma}$.
- The variations around the mean for each of the responses are controlled by the diagonal elements of $\boldsymbol{\Sigma}$.
- The smooth/rapid changes of the responses across the input space are controlled by $\boldsymbol{\omega}$.

To demonstrate the above features, the example in Fig. 4 is recalled. Therein, the three mean values of the responses (the dashed gray lines) are set to $\boldsymbol{\beta} = [55, 0, 5]$. In Fig. 4(b), the symmetric 3×3 matrix $\boldsymbol{\Sigma}$ is diagonal with small (positive) entries. This choice of $\boldsymbol{\Sigma}$ results in small variations around the mean at a fix input location for any of the responses. To have smooth random fields, ω is set to a small number as well. To increase the variations around the mean (corresponding to Fig. 4(c)), the diagonal elements of $\boldsymbol{\Sigma}$ are increased. To prescribe negative (positive) correlation between realizations of v and φ (see Fig. 4(d)), the corresponding element in $\boldsymbol{\Sigma}$ is set to a negative (positive) number (while ensuring $\boldsymbol{\Sigma}$ is still positive definite). Lastly, to decrease the smoothness of the fields over the input space (see Fig. 4(e)), ω is increase.

In case some experimental data are available, all the hyperparameters of an MRGP model can be estimated via, e.g., the maximum likelihood method. Otherwise, as in this work, expert or prior knowledge can be used to adjust these parameters and model a spatially varying quantity. Once these hyperparameters are determined, generating realizations from an MRGP model is achieved through some closed form formula (detailed in Appendix A.1).

3.2. Top-down sampling for uncertainty propagation

To carry out one multiscale simulation, material properties must be assigned to all the IPs at all scales where the IP properties at any scale depend on an RVE at the next finer scale (this RVE itself has many IPs). Since these properties depend on the uncertainty sources (or, equivalently, on the RFs), the latter must be coupled across the scales. Recall that, due to the multiscale nature of the structure, the number of RFs significantly increases at the fine-scales because we associate an RF to *each* structure realization. For instance, in the two-scale structure in Fig. 3 there will be $10\,000 + 1$ RFs; one for the mesostructure and 10 000 for its IPs (corresponding to the microstructures). The mesoscale RF will, in essence, characterize the spatial variations of the microscale RFs.

Having used RFs whose parameters are physically sensible and can be directly linked to the uncertainty sources, this cross-scale coupling is straightforward and can be achieved with top-down sampling where the *outputs* of the MRGP at each IP of a particular scale serve as the *hyperparameters* of the MRGP of the RVE associated with that IP. This process constitutes *nested* RFs. To assign values to the IP parameters in the entire multiscale structure, this approach starts from the coarsest or top scale and hence the name top-down sampling. In the above example, the mesoscale MRGP is first used to assign values to the mesoscale IPs which essentially assigns values to the hyperparameters of the 10 000 MRGPs at the microscale. Then, these latter MRGPs are used to assign values to the IPs of each microstructure.

While the top-down sampling method works with any parametric RF representation (e.g., PCE or KL expansion), we highly recommend employing compact representations that include a few hyperparameters. This is mainly because the number of hyperparameters at the coarse scales increases rapidly as the number of spatially varying quantities increases at the fine scales. For instance, assuming three (two) quantities change spatially in the $3D$ microstructure in Fig. 3, an MRGP with 12 (8) hyperparameters is required. To model the spatial variations of these 12 (8) hyperparameters at the mesoscale, an MRGP with 93 (47) hyperparameters is required.
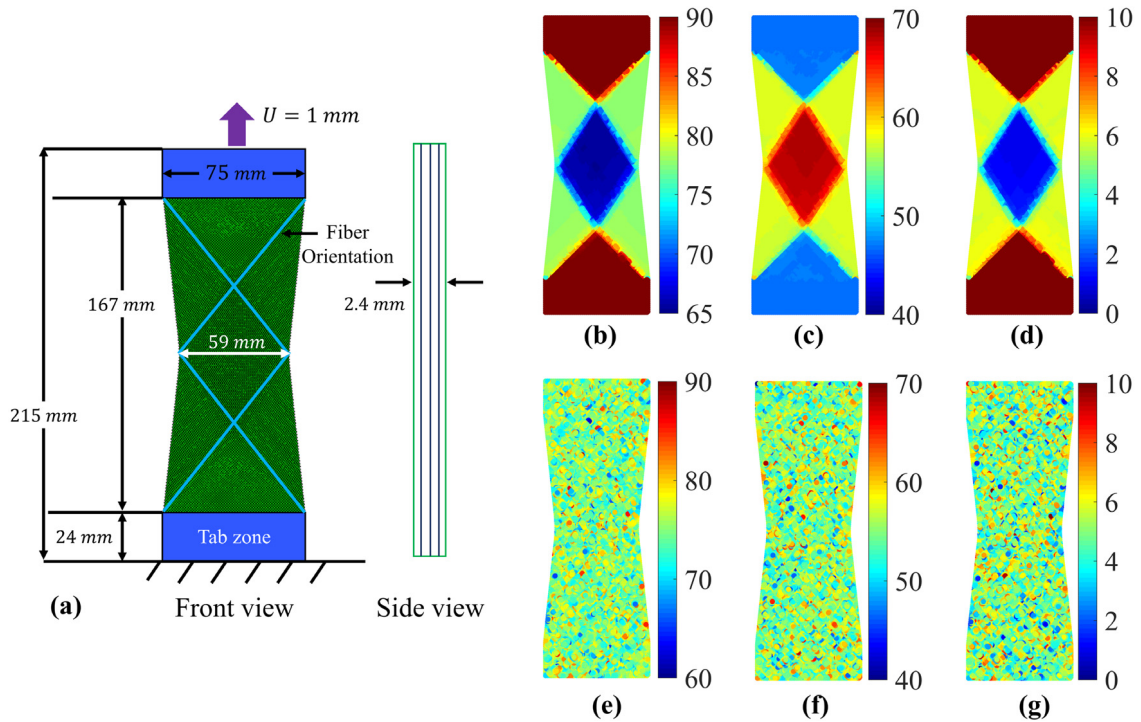
Fig. 6. (Color online) The macroscopic cured woven laminate structure studied in our work: (a) The undeformed structure consists of four identical plies and undergoes bias tension deformation. The bottom end of the sample is clamped while the other end is pulled by 1 mm. The light blue lines indicate the fiber orientation. The dimensions are scaled for a clearer representation. The contour plots in (b) through (g) demonstrate sample spatial variations in yarn angle ((b) and (e), in degrees), fiber volume fraction ((c) and (f), in percent), and fiber misalignment angle ((d) and (g), in degrees) across the IPs. Contours (b) through (d) and (e) through (g) correspond to, respectively, cases 10 and 8 in Section 4.6.

4. Application of the proposed approach in cured woven fiber composites

As argued in Section 1, woven fiber composites possess a hierarchical structure where multiple sources of uncertainty exist across the scales. In this section, we follow the steps of our approach to quantify the macroscale uncertainty in the elastic response of a cured woven composite as a function of spatial variations in the fiber volume fraction (microscale and mesoscale), yarn angle, and fiber misalignment angles (mesoscale). As illustrated in Fig. 6(a), the structure is composed of four identical woven plies that are stacked in the same orientation and constitute a total thickness of 2.4 mm (the fiber orientations are indicated with light blue lines). The geometry of these woven plies are obtained via the bias-extension simulation of dry woven fabrics using the non-orthogonal constitutive preforming model. While the bottom of the sample is clamped, the other end is pulled by 1 mm to generate the bias tension deformation. In the macroscale simulations, $3D$ solid continuum elements are employed to discretize the structure. As our focus is on UQ and UP, at this point we have assumed that only elastic deformation occurs. For brevity, we denote the three scales with numbers throughout this section: $1 \rightarrow Macro, 2 \rightarrow Meso, 3 \rightarrow Micro$.

4.1. Uncertainty Sources: Yarn Angle, Fiber Volume Fraction, and Fiber Misalignment Angles

The yarn material properties primarily depend on two parameters: fiber volume fraction, v, and fiber misalignment. While in most previous works v is postulated to be spatially constant [92–94], in practice, it varies along the yarn path particularly where yarns have compact contact [28,29]. Consequently, our first uncertainty source arises from the spatial variations of v which starts from the microscale and propagates to mesoscale and macroscale. In this work, we have assumed that $45\% \leq v \leq 65\%$ based on the test of our material system. Fig. 6(c) and (f) demonstrate two possible spatial variations for v over the macrostructure.

$\vec{g}_k$: Local orthogonal frame on the yarn cross-section

$\vec{g}_1$: Tangent direction of the yarn center axis

$\vec{f}_1$: Individual fiber direction with respect to $\vec{g}_k$ frame

$[\theta, \varphi]$: Zenith and azimuth angles of $\vec{f}_1$ in $\vec{g}_k$ frame
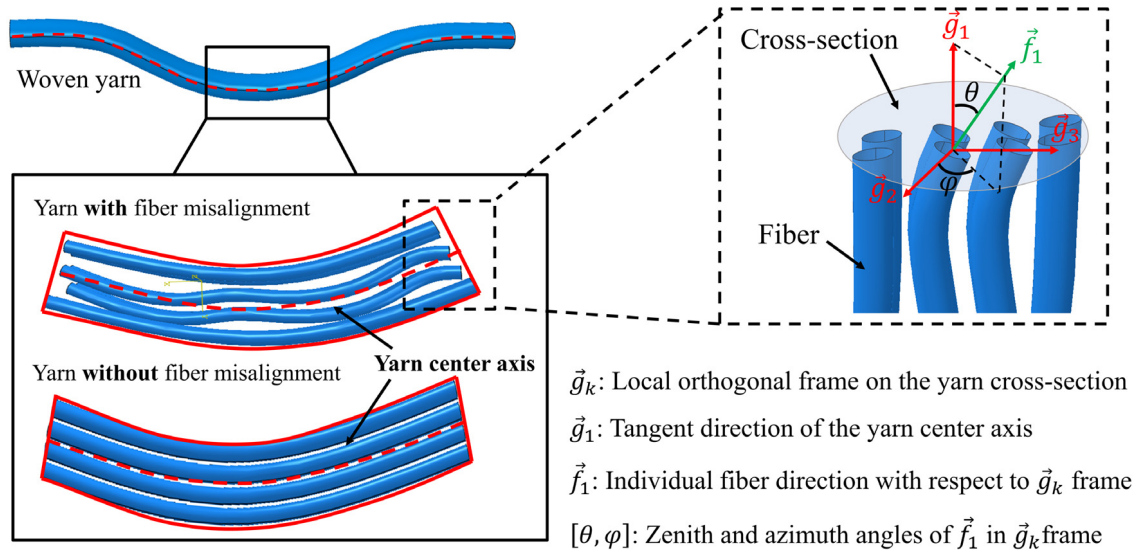
Fig. 7. (Color online) Fiber misalignment angles: The zenith and azimuth angles characterize the fiber misalignment angle with respect to the local orthogonal frame on the yarn cross-section.

During the manufacturing process, the fibers in the yarn deviate from the ideal orientation and render the cross-section of the yarn heterogeneous and anisotropic. These deviations result in fiber misalignment which is different from the concept of fiber waviness in that a fiber can be perfectly waved without misalignment. As illustrated in Fig. 7, this misalignment can be characterized with the two angles $-\pi \leq \varphi \leq \pi$ and $0° \leq \theta \leq 90°$ which measure the deviation of the fiber direction, f_1, with respect to the local orthogonal frame on the yarn cross-section, g_k. Based on the available experimental data in the literature [28], in this work we have assumed $-\pi \leq \varphi \leq \pi$ and $0° \leq \theta \leq 90°$. Fig. 6(d) and (g) demonstrate two possible spatial variations for θ over our macrostructure.

Lastly, we note that in modeling the mesoscale woven composites the yarn angle (α, the angle between the warp and the weft, see Fig. 2(a)) is often presumed to be $90°$. This assumption does not generally hold in practice due to the large in-plane shear deformation during preforming process and manufacturing imperfections. Hence, we also investigate the effect of the spatial variations of mesoscale yarn angle on the macroscopic properties. In our example, as opposed to the other three parameters (i.e., $[v, \varphi, \theta]$), the spatial variation of α in the macroscale can be obtained from the preforming process simulation [95]. So, we investigate the effect of α in two cases: deterministic spatial variations (see Fig. 6(b)) and stochastic spatial variations (see Fig. 6(e)).

4.2. Multiscale finite element simulations

We employ the computational homogenization technique for modeling the multiscale woven sample where the material property at any length-scale is calculated through the homogenization of an RVE at the lower scale. Below, we elaborate on the details of FE simulations at each scale. It is noted that while in traditional multiscale homogenization it is assumed that macroscale and mesoscale IPs represent the same microstructure, we assign different microstructures to each IPs at each length-scale.

At the microscale, the RVEs consist of $300 \times 300 \times 60$ voxels ($42\ \mu m \times 42\ \mu m \times 8.4\ \mu m$) and the fibers have a diameter of $7\ \mu m$ (see Fig. 8). The simulations are elastic where periodic boundary conditions are employed. It is assumed that the fibers and the matrix are well bonded and there are no voids. To obtain the stiffness matrix, C, of the UD RVE, six stress-free loading states are applied (i.e., only one of the ε_{xx}, ε_{yy}, ε_{zz}, ε_{xy}, ε_{xz}, and ε_{yz} strain components are applied in each case). Since the simulations are elastic, C mainly depends on the volume fraction, v [96].

At the mesoscale, the open source software *TexGen* [30] is used to create the geometry and mesh for the 2×2 twill woven RVE (see Fig. 2(a)) with 8 yarns. To generate such an RVE in *TexGen* the yarns' paths, cross-sections,
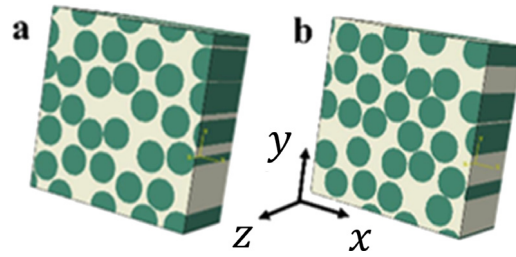
Fig. 8. (Color online) Sample UD RVEs at the microscale: Two UD RVEs with randomly distributed fibers. Both RVEs have periodic boundaries and a volume fraction, v, of 58%. These UD RVEs correspond to mesoscale IPs and their deviation from the yarn centerline models fiber misalignment.

and the weaving patterns must be prescribed. Yarns' paths in *TexGen* are represented by $3D$ spatial curves and their cross-sections are defined as $2D$ ellipses perpendicular to the tangent of yarn centerline. The space between the yarns is filled with matrix and voxel meshes are used to discretize the RVE where each voxel is designated to either a yarn or the matrix. To balance cost and accuracy, we have used a voxel mesh with 625 000 elements. To reduce the computation costs, periodic boundary conditions (PBCs) are employed throughout. We note that, if PBCs are prescribed correctly, the homogenized stress–strain response does not scale with the RVE size [96].

Properties of carbon fibers and epoxy resin were taken from manufacturer's data (see Table 1). The resin is isotropic and its material properties are taken from pure epoxy. Yarns with well-aligned fibers are treated as transversely isotropic. With fiber misalignment, however, yarns are not transversely isotropic since the material frame across the IPs on their cross-section is non-uniformly distributed. In this case, the micro-plane triad model proposed by Kedar et al. [97] is employed to account for fiber misalignment by defining an orthotropic micro-triad, $\vec{f}_k$, for each IP of the yarn. This triad is related to the local frame, $\vec{g}_k$ (see Fig. 7), via the misalignment angles:

$$\vec{f}_1 = \cos(\theta)\frac{\vec{g}_1}{|\vec{g}_1|} + \sin(\theta)\cos(\varphi)\frac{\vec{g}_2}{|\vec{g}_2|} + \sin(\theta)\sin(\varphi)\frac{\vec{g}_3}{|\vec{g}_3|}, \tag{4.1}$$

$$\vec{f}_2 = -\sin(\theta)\frac{\vec{g}_1}{|\vec{g}_1|} + \cos(\theta)\cos(\varphi)\frac{\vec{g}_2}{|\vec{g}_2|} + \cos(\theta)\sin(\varphi)\frac{\vec{g}_3}{|\vec{g}_3|}, \tag{4.2}$$

$$\vec{f}_3 = \vec{f}_1 \wedge \vec{f}_2, \tag{4.3}$$

where $|\cdot|$ and $\wedge$ denote, respectively, the norm of a vector and the cross product. As for the local frame $\vec{g}_k$, it is automatically generated by *TexGen* for each IP (each voxel at the mesoscale) once the woven RVE is discretized. We note that, the stiffness matrix at each yarn material point is obtained via the UD-RVE homogenization (see also Fig. 14).

To link the mesoscale and macroscale, the stress–strain relations for effective elastic material properties of woven RVE are required. This relation can be written in terms of the symmetric mesoscale stiffness matrix as:

$$\begin{bmatrix} \sigma_{11} \\ \sigma_{22} \\ \sigma_{33} \\ \sigma_{12} \\ \sigma_{13} \\ \sigma_{23} \end{bmatrix} = \begin{bmatrix} C_{11} & C_{12} & C_{13} & C_{14} & 0 & 0 \\ & C_{22} & C_{23} & C_{24} & 0 & 0 \\ & & C_{33} & C_{34} & 0 & 0 \\ & & & C_{44} & 0 & 0 \\ & Sym. & & & C_{55} & C_{56} \\ & & & & & C_{66} \end{bmatrix} \begin{bmatrix} \varepsilon_{11} \\ \varepsilon_{22} \\ \varepsilon_{33} \\ 2\varepsilon_{12} \\ 2\varepsilon_{13} \\ 2\varepsilon_{23} \end{bmatrix}, \tag{4.4}$$

where coordinate 3 is in the thickness direction of the woven RVE (see Fig. 2(a)). If $\alpha = 90°$, coordinates 1 and 2 coincide with the warp and weft directions and the effective material behavior can be described with an orthotropic material model. If $\alpha \neq 90°$, a monoclinic material model is used instead.

4.3. Top-down sampling, coupling, and random field modeling of uncertainty sources

To help clarify the descriptions, we first introduce some notation. Superscript and subscripts denote, respectively, scales and IPs. Variables with a bar represent averaged quantities over all the IPs at a particular scale. For instance,

Table 1
Fiber and matrix properties: The moduli (i.e., E and G) are all in GPa. See Fig. 8 for the definition of coordinate system.

	E_{zz}	$E_{xx} = E_{yy}$	$v_{zx} = v_{zy}$	v_{xy}	$G_{xz} = G_{yz}$	G_{xy}
Carbon fiber	245	19.8	0.28	0.32	29.2	5.92
Epoxy resin	3.79	3.79	0.39	0.39	1.36	1.36
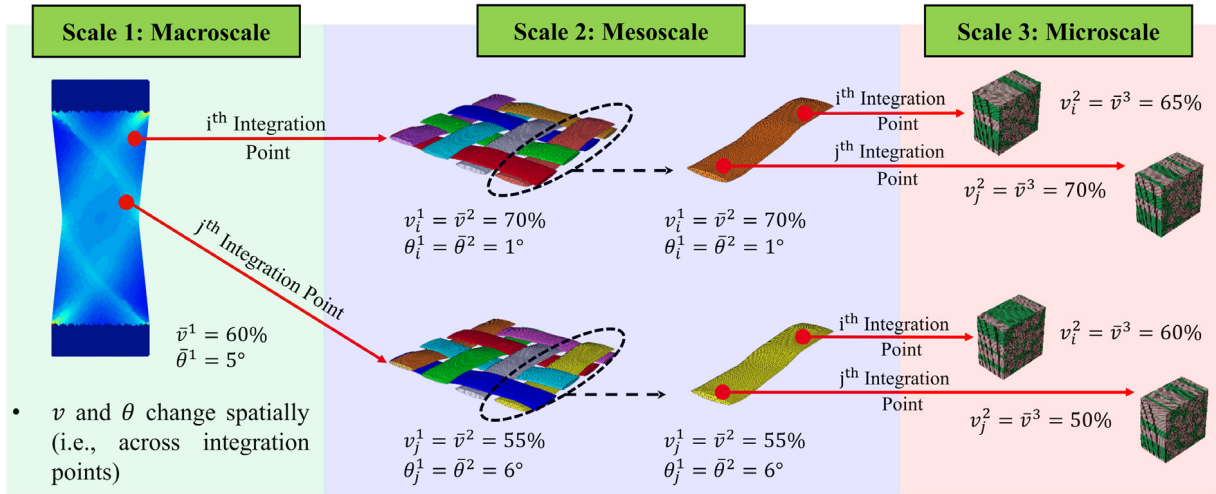
Fig. 9. (Color online) Coupling the uncertainty sources across the scales: The spatial variations of v and θ at the macroscale are connected to those at the finer scales. For brevity, the coupling is illustrated only for the average values for the two quantity (i.e., the mean of the RFs: $\beta = [\beta_v, \beta_\theta] = [\bar{v}^2, \bar{\theta}^2]$). The same method applies to other parameters of the random field (β_φ, Σ, and). The macrostructure contains 15 000 IPs. Each mesoscopic woven RVE contains 625 000 IPs where 525 000 IPs belong to the eight tows and the rest to the matrix.

v_i^1 denotes the fiber volume fraction assigned to the ith IP at the macroscale. $\bar{\theta}^2 = \sum_{i=1}^{N} \theta_i^2$ represents the average misalignment (zenith) angle at the mesoscale for a woven RVE.

At the microscale, the average volume fraction is the only source of uncertainty. Since the spatial distribution of the fibers in a UD-RVE has negligible effect in linear analyses, there is no need for RFs at this scale. At the mesoscale and macroscale, however, the fiber volume fraction and the two misalignment angles change spatially and hence RFs must be employed for modeling them. As motivated in Section 3, MRGPs were employed to model all the spatial variations (other RF representations can also be used in the expense of more computations).

Assuming the eight tows in a woven RVE are statistically independent and the spatial variations within them originate from the same underlying random process [27], a total of 12 hyperparameters are required to completely define an MRGP for a woven RVE (see Eq. (4.5)): three mean values ($\beta = [\beta_v, \beta_\varphi, \beta_\theta]^T$), six variance/covariance values for Σ ($[\sigma_{vv}^2, \sigma_{\varphi\varphi}^2, \sigma_{\theta\theta}^2, \sigma_{v\varphi}^2, \sigma_{v\theta}^2, \sigma_{\varphi\theta}^2]$), and three roughness parameters ($\omega = [\omega_x, \omega_y, \omega_z]^T$ where xyz denotes the cartesian coordinate system at the mesoscale). Once these parameters are specified, the spatial coordinates of the IPs in a woven RVE can be used to assign realizations of v, φ, and θ to them (see Appendix). For each IP at the macroscale, however, these 12 hyperparameters serve as the responses of the macroscale MRGP which has a total of 93 hyperparameters (12 mean values for β, 78 unique covariance/variance values for Σ, and 3 values for $\omega = [\omega_\eta, \omega_\xi, \omega_\zeta]^T$ where $\eta\xi\zeta$ denotes the cartesian coordinate system at the macroscale). In the top-down sampling approach, first the 48 hyperparameters of the macroscopic MRGP are prescribed. Then, this MRGP is sampled to assign 12 hyperparameters to each macroscopic IP where they are used in the mesoscopic MRGPs. This process is illustrated in Fig. 9 where, for clarity, only two (out of the 12) hyperparameters at the mesoscale are presented.

We note that some parameters might not spatially vary according to a normal distribution. In such cases, we recommend using appropriate transformations to convert the distribution into a Gaussian one. For instance, the zenith misalignment angle has a log-normal distribution [28] and so we carry out all the computations in the log-space and then revert to the original scale via exponentiation. If transformation is not possible, non-Gaussian RFs (see Section 2.1.2) can be used in the top-sampling procedure. Sample spatial variations of v^2, φ^2, and θ^2 over the woven
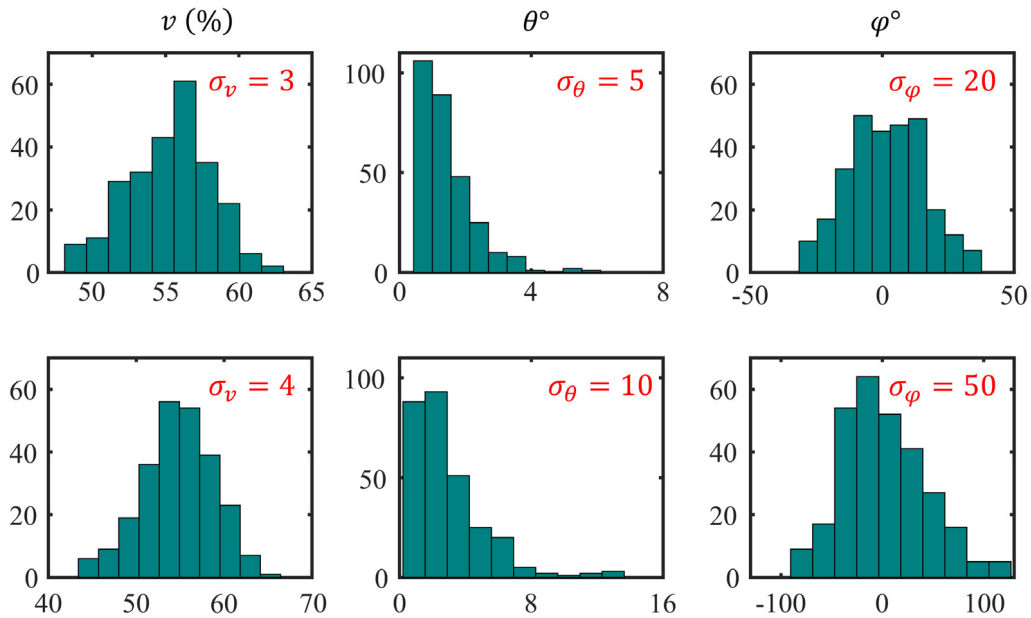
Fig. 10. Sample spatial variations of v^2, φ^2, and θ^2 for different variances: The spatial variations belong to a randomly selected cross-section of a yarn with the averages of 55%, 3°, and 0°, respectively. The distribution of θ^2 is log-normal.

RVE are illustrated in Fig. 10. Such variations are controlled by adjusting the parameters of the MRGP (see Section 3.1 and Appendix A.2).

4.4. Dimension reduction at the mesoscale via sensitivity analysis

By modeling the spatial variations via RFs, the dimensionality of the UQ and UP problem has decreased to the number of RF hyperparameters. Although this is a significant reduction, the considerable cost of multiscale simulations (even in the linear analysis) renders the UQ and UP process computationally demanding. To address this issue, we note that depending on the property of interest a subset of uncertainty sources are generally the dominant ones in physical systems. Since our composite undergoes an elastic deformation, we expect a small subset of the uncertainty sources (i.e., RF hyperparameters) to be important.

We conducted multiscale sensitivity analyses to determine which of the 12 hyperparameters of an MRGP model are the most important ones (and must be considered in UP) based on their impact on mesoscale material response. Our studies consisted of changing one of the hyperparameters while keeping the rest of them fixed. Then, if the variations in the homogenized response (effective moduli) were negligible, the hyperparameter was deemed as insignificant and set to a constant thereafter. For brevity, we summarize the results below and include the details in Appendix A.2. All the simulations in this section were conducted on a woven RVE with $\alpha = 90°$.

We found that the *homogenized moduli* (see Eq. (4.4)) are affected by neither the six covariance/variance values (i.e., $\left[\sigma_{vv}^2, \sigma_{\varphi\varphi}^2, \sigma_{\theta\theta}^2, \sigma_{v\varphi}^2, \sigma_{v\theta}^2, \sigma_{\varphi\theta}^2\right]$) nor the three roughness parameters $\boldsymbol{\omega} = \left[\omega_x, \omega_y, \omega_z\right]^T$. In case of average values (i.e., $\boldsymbol{\beta}$), the average fiber volume fraction ($\bar{v}$) and zenith angle ($\bar{\theta}$), as opposed to that of the azimuth angle, were found to considerably affect the homogenized response of a woven RVE at the mesoscale. The effect of average values on the effective moduli are summarized in Fig. 11.

It must be noted that since we are interested in the elastic response of the multiscale composite in Fig. 6, the variations of *effective* moduli were only considered in our sensitivity studies. As opposed to the effective behavior, the local behavior (i.e., stress field) of the woven RVE is quite sensitive to the spatial variations of both v and θ (but not φ) and must be considered in nonlinear analysis, see Fig. 12.
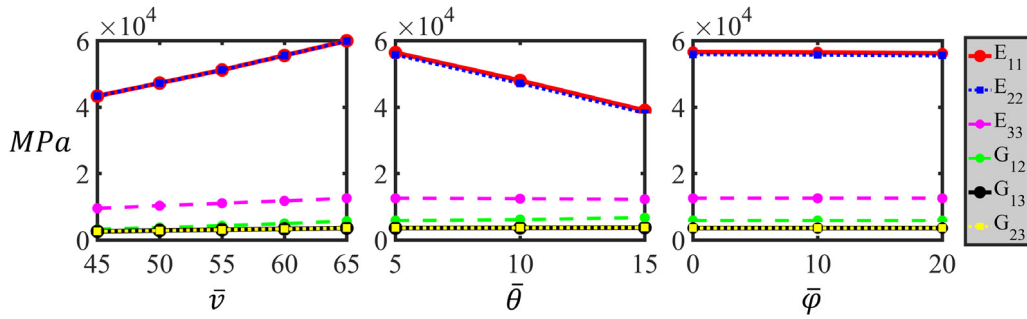
Fig. 11. (Color online) Effect of average values on the effective moduli of a woven RVE: While the average fiber volume fraction ($\overline{v}$) and zenith angle ($\overline{\theta}$) considerably affect the homogenized response of a woven RVE at the mesoscale, the average and spatial distribution of azimuth angle are unimportant. See Fig. 2(a) for the definition of the coordinate system. Each point on these figures represents an averaged value over 30 multiscale simulations (see Appendix A.2 for the details). The yarn angle is set to 90°.
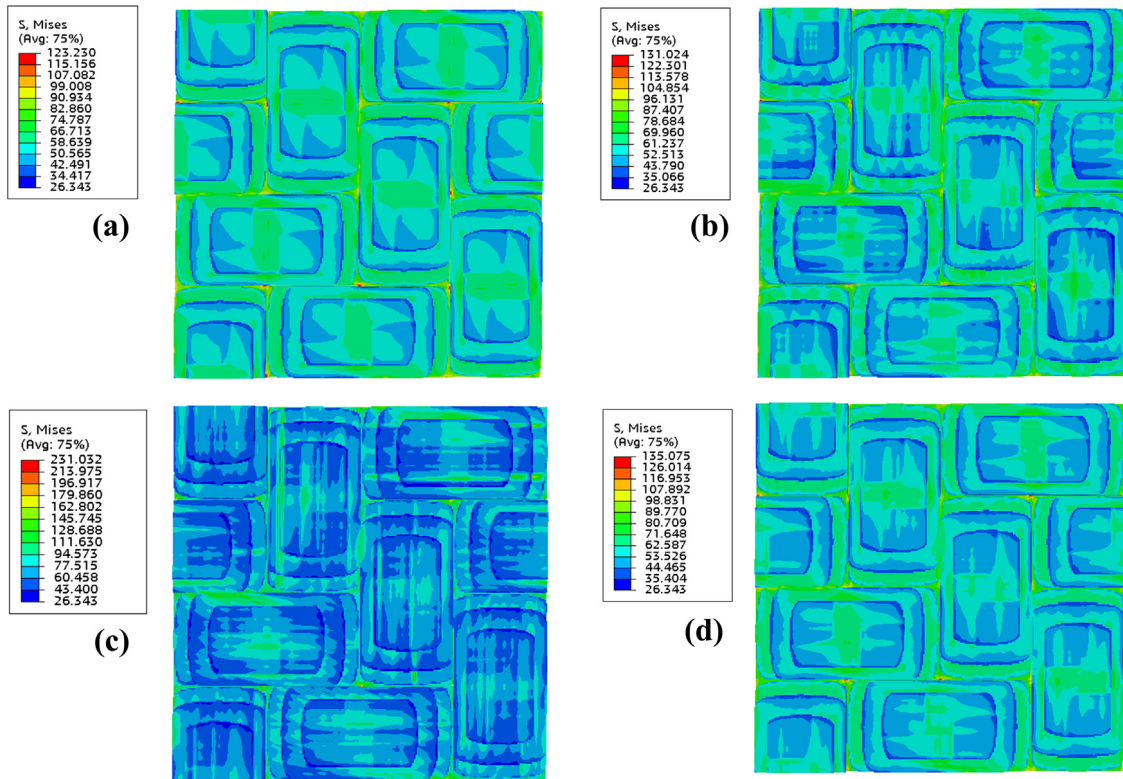
Fig. 12. (Color online) Effect of spatial variations on the stress field (MPa): Stress fields for (a) No fiber misalignment and no spatial variations in v. (b) Only spatial variations in v where $\sigma_{vv}^2 = 16\%$ and $\omega = 1$. (c) Only spatial variations in φ and θ where $\overline{\varphi} = 0°$, $\overline{\theta} = 15°$, $\sigma_{\varphi\varphi}^2 = 2500$, $\sigma_{\theta\theta}^2 = 2$, $\omega_\theta = 1$, and $\omega_\varphi = 1$. (d) Same settings as in (c) but with $\overline{\theta} = 2°$ and $\sigma_{\varphi\varphi}^2 = 400$. In all simulations, $\overline{v} = 65\%$.

4.5. Replacing meso and microscale simulations via metamodels

To further reduce the multiscale UQ and UP costs, we employ a metamodel to replace the micro and mesoscale FE simulations corresponding to each macroscale IP. In particular, the metamodel captures the macroscale spatial variations of the stiffness matrix (see Eq. (4.4)) of the woven RVEs associated with the macroscale IP's as a function of yarn angle (α^2), average volume fraction ($\overline{v}^2$), and average misalignment angle ($\overline{\theta}^2$). In machine learning parlance,
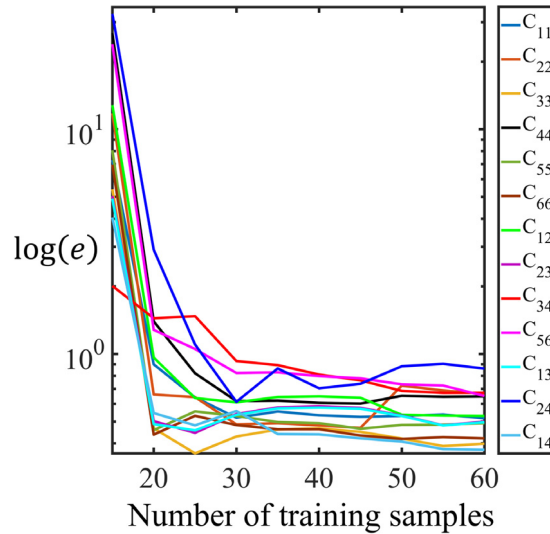
Fig. 13. (Color online) Prediction error (log scale) as a function of the number of training samples: As the number of training samples increases, the accuracy of the MRGP metamodel in predicting the elements of the stiffness matrix of the mesoscale woven RVE increases.

the inputs and outputs of the metamodel are, respectively, $[\alpha^2, \overline{v}^2, \overline{\theta}^2]$ and the stiffness matrix of a woven RVE. We note that if the mesoscale spatial variations of the fiber volume fraction and misalignment angle were found to be important in Section 4.4, the metamodel would have had the corresponding hyperparameters of the MRGP (e.g., σ_{vv}^2 and $\sigma_{\theta\theta}^2$) as inputs.

To fit the metamodel, we generated 6 training datasets of sizes $10, 20, \ldots, 60$ with Sobol sequence [98,99] for $\alpha^2 \in [60°, 90°]$, $\overline{v}^2 \in [45\%, 70\%]$, and $\overline{\theta}^2 \in [0°, 15°]$. Afterwards, we fitted an MRGP metamodel to each dataset. The accuracy of each model was then evaluated against a validation dataset with 20 samples via:

$$e = 100 \sqrt{\frac{1}{20} \sum_{i=1}^{20} \left(1 - \frac{\hat{y}}{y}\right)^2} \%. \tag{4.5}$$

The prediction error of each model is illustrated in Fig. 13 where it is evident that with roughly 30 samples all the elements of C can be predicted with less than 1% error.

4.6. Results on macroscale uncertainty

Multiple macro simulations are conducted where α_i^1, v_i^1, and θ_i^1 change spatially across the macroscale IPs in each simulation and the fitted metamodel is used to predict the stiffness matrix of the woven RVEs associated with these IPs. To quantify the importance of these variables and their spatial variations on the macroscopic behavior, ten cases are considered. As detailed in Table 2, the spatial variations are changed in a controlled manner from one case to the next. Other than the first two cases, 30 independent macroscale simulations are conducted for each case to account for the randomness. In summary, a total of 242 macroscale simulations were conducted with an average simulation time of roughly 20 min running on an HPC cluster with 8 nodes per simulation. In all simulations, the average fiber volume fraction in the macrostructure (i.e., $\overline{v}^1$) and the yarn volume fraction in woven RVE were, respectively, 55% and 84%. Additionally, since $\overline{\alpha}^1$ from processing simulation was 78° (see Fig. 6(b) for the spatial distribution), in cases where α_i^1 changed spatially, it was ensured that the average over all the IPs was 78°. In cases with fiber misalignment (i.e., non-zero $\overline{\theta}^1$), the average over all the IPs was always set to 5°. The variance/covariance elements of the marginal variance matrix (i.e., Σ) of the macroscale MRGP model were set to: $\left[\sigma_{\alpha\alpha}^2, \sigma_{vv}^2, \sigma_{\theta\theta}^2, \sigma_{\alpha v}, \sigma_{\alpha\theta}, \sigma_{v\theta}\right] = [14, 16, 2.25, -4, 4, -4]$. These values were chosen to model sufficient variations around the mean values (i.e., β) while ensuring the resulting random values are valid (e.g., $\theta_i^1 \geq 0°$ and $\alpha_i^1 \leq 90°$) and fall in the range were the mesoscale metamodel is

Table 2
Description of the simulation settings: Ten simulation cases are considered to quantify the macroscale uncertainties and the relative importance of local fiber volume fraction, yarn angle, and fiber misalignment angle. The variations are changed in a controlled manner from case to case. MRGPs are employed to generate random realizations in all cases.

	Description
Case 1	**1 simulation:** No misalignment, no spatial variations in v^1 and α^1, $\overline{v}^1 = 55\%$ and $\overline{\alpha}^1 = 90$
Case 2	**1 simulation:** No misalignment, no spatial variations in v^1 and $\overline{v}^1 = 55\%$, α^1 from processing simulations
Case 3	**30 simulations:** No misalignment, no spatial variations in v^1 and $\overline{v}^1 = 55\%$, α^1 changes spatially via GP
Case 4	**30 simulations:** No misalignment, spatial variations in v^1 via GP and $\overline{v}^1 = 55\%$, no spatial variations in α^1 and $\overline{\alpha}^1 = 90$
Case 5	**30 simulations:** No misalignment, spatial variations in v^1 via GP and $\overline{v}^1 = 55\%$, α^1 from processing simulations
Case 6	**30 simulations:** $\overline{\theta}^1 = 5$ and spatial variations with GP, no spatial variations in v^1 and α^1, $\overline{v}^1 = 55\%$ and $\overline{\alpha}^1 = 90$
Case 7	**30 simulations:** $\overline{\theta}^1 = 5$ and spatial variations with GP, no spatial variations in v^1 and $\overline{v}^1 = 55\%$, α^1 from processing simulations
Case 8	**30 simulations:** There is misalignment and α^1, v^1 and θ^1 change spatially via an MRGP (uncorrelated changes)
Case 9	**30 simulations:** There is misalignment and α^1, v^1 and θ^1 change spatially via an MRGP (correlated changes)
Case 10	**30 simulations:** There is misalignment where v^1 and θ^1 change spatially via an MRGP (changes are correlated and conditioned on the spatial variations of α^1 from processing simulations, see Appendix A.3)

fitted. To eliminate the spatial variations of any of the parameters (e.g., $\overline{v}^1$ and $\overline{\theta}^1$ in case 3), the corresponding variances/covariances in Σ were simply set to zero (this will essentially reduce the MRGP model to a single response GP). Finally, we note that $\sigma_{\alpha v}$ is negative to model the increase in fiber volume fraction as the yarns get closer after preforming. $\sigma_{v\theta}$ is also negative to consider the decrease in misalignment angle in rich fiber regions [28].

Our multiscale UP process is summarized in Fig. 14. For each simulation in Table 2, first the macroscopic spatial variations of the IP parameters (i.e., $\alpha_i^1, v_i^1, \theta_i^1$) are prescribed via the macroscale MRGP model. These parameters correspond to the hyperparameters of the mesoscale MRGP model (associated with each macroscale IP) that assigns parameters to the mesoscale IPs. Finally, a microstructure is assigned to each mesoscale IP where its average fiber volume fraction is determined by the mesoscale MRGP. For our example in Fig. 6(a), the integrated micro and mesoscale simulations are replaced with a GP metamodel that is used to predict the stiffness matrix at each different location in the macroscale simulation.

Fig. 15(a) compares the exerted force on the cross-section of the sample for the ten cases where, for cases 3 through 10, the force–displacement line is averaged over the 30 multiscale simulations. It is evident that with spatial variations, especially in α, a larger force is exerted on the cross-section of the sample. In particular, the three bottom lines in Fig. 15(a) correspond to the cases where there are no spatial variations in the yarn angle (cases 1, 4, and 6). Fig. 15(b) demonstrates the standard deviation of the 30 simulations for cases 3 through 10. As it can be observed, the global response of the structure is not noticeably sensitive to the spatial variations.

The force–displacement curve is a global measure of the structure's behavior. To illustrate the effect of spatial variations on local behavior, we compare the average and standard deviation of the von-Mises stress field in Figs. 16 and 17, respectively. By comparing the stress fields for cases 1 through 3 in Fig. 16 we can conclude that spatial variations of the yarn angle are significantly important and must be considered. Additionally, the random spatial variations of yarn angle (see case 3 in Fig. 17) can affect the stress fields (though quite insignificant when comparing the magnitudes of the color bars in Figs. 16 and 17). The effect of spatial variations in fiber volume fraction and misalignment angle can be quantified by comparing cases 4 through 7 where it is demonstrated that these effects are quite negligible with respect to the effect of the yarn angle. Similar results are obtained in cases 7 through 10
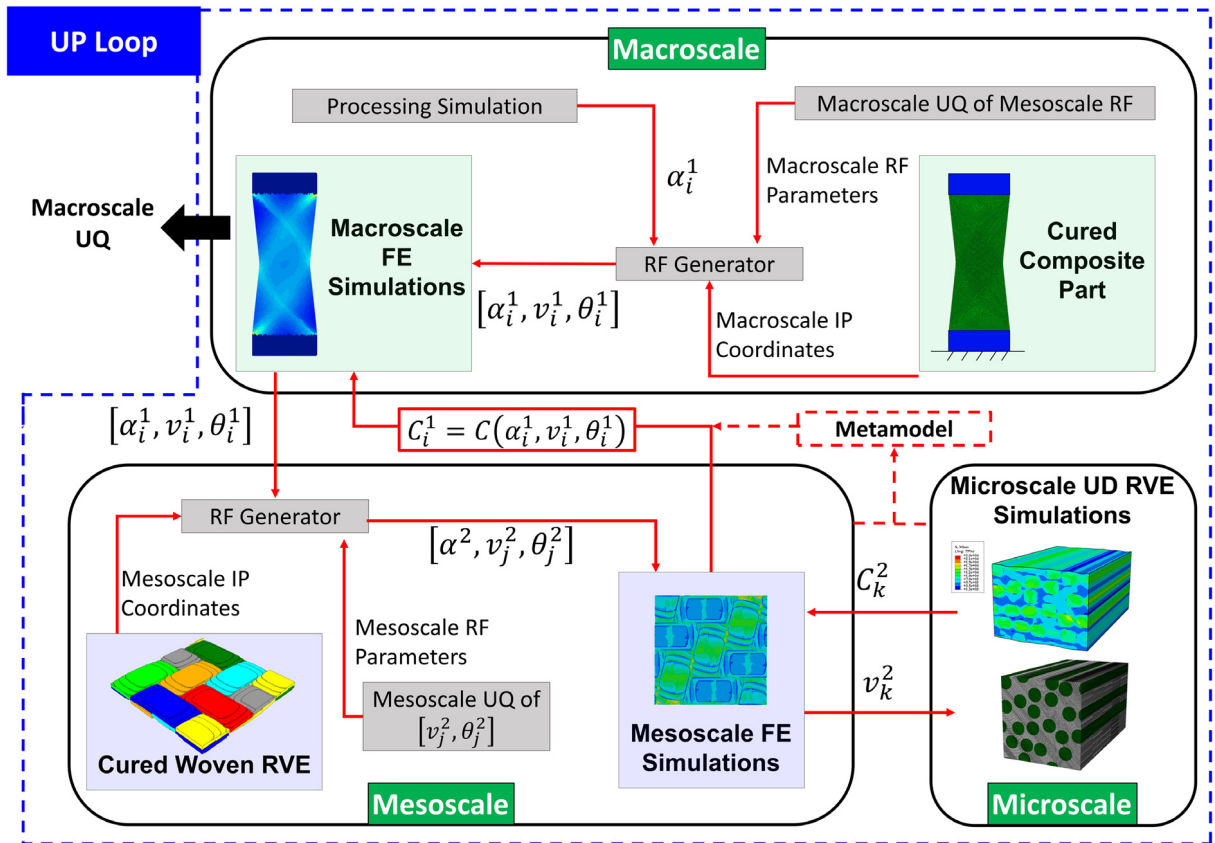
Fig. 14. (Color online) Multiscale UQ and UP in a woven fiber composite: During the UP process, various macroscale simulations are conducted where the spatial distributions of fiber volume fraction and misalignment angle vary among different simulations. These spatial distributions are, in cases 9 and 10, conditioned on that of the yarn angle (which is obtained from the processing simulation). The top-down sampling approach is used for passing the spatial distributions from the macroscale down to the mesoscale. To reduce the computational expense of nested FE simulations, the microscale and mesoscale simulations are replaced with a metamodel.

where most of the variations can be attributed to the yarn angle. In particular, the mean stress field in case 10 (which is perhaps the most relevant to a real part) significantly deviates from that of the reference solution in case 1. The variations among the 30 simulations in case 10 are not, however, the most significant among all the cases because the spatial variations of the yarn angle are fixed across the 30 simulations. The most variations across the simulations belong to case 9 (where all the three parameters change spatially and randomly) followed by case 3 (where only the yarn angle changes spatially and randomly).

Since we have employed an explicit solver in our FE simulations, artificial stress concentrations might occur especially at both ends of the sample. For this reason, in Fig. 18 the mean and standard deviation of the stress along the mid-section of the part are plotted. In line with the above discussions it is observed that the stresses are quite significantly underestimated when the spatial variations in the yarn angle are not considered (cases 1, 4, and 6 in Fig. 18). The most variations also belong to case 9 followed by case 3. Finally, we note that the zigzag pattern in the stresses in Fig. 18 are due to the rough changes in the yarn angle in the adjacent macroscale IPs (and not the severe distortion of the finite elements).

5. Conclusion and Future Works

Limited advancement has been made in integrating statistical uncertainty quantification (UQ) and propagation (UP) methods with multiscale simulations. Herein, we have introduced an approach for multiscale UQ and UP that models the uncertainty sources with multi-response Gaussian processes (MRGPs) and employs statistical techniques
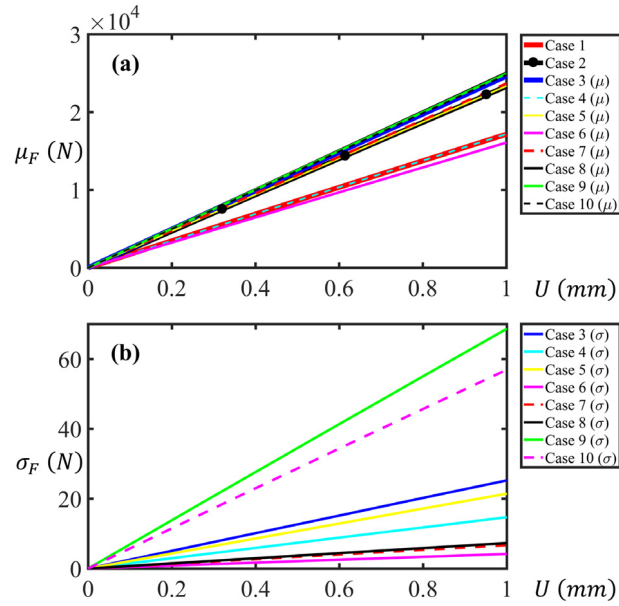
Fig. 15. (Color online) Effect of spatial variations on force–displacement curves: (a) Average and (b) standard deviation. Without any spatial variations, a smaller force is applied to the cross-section of the woven fiber composite. For cases 3 through 10, the curve is averaged over 30 multiscale simulations.
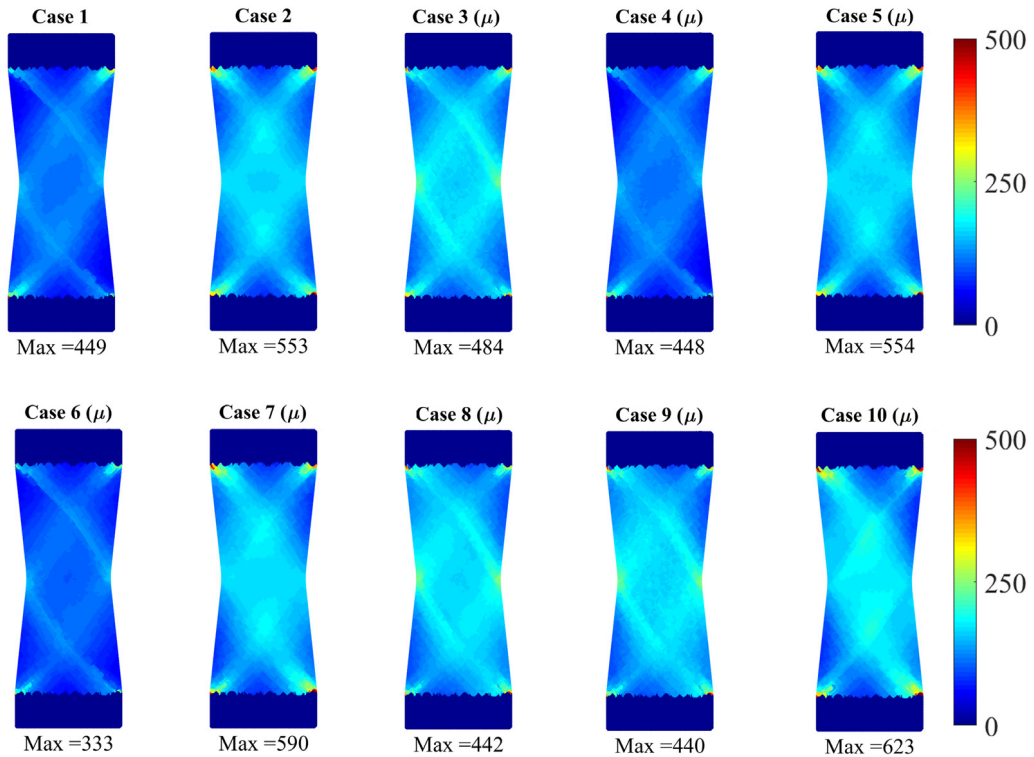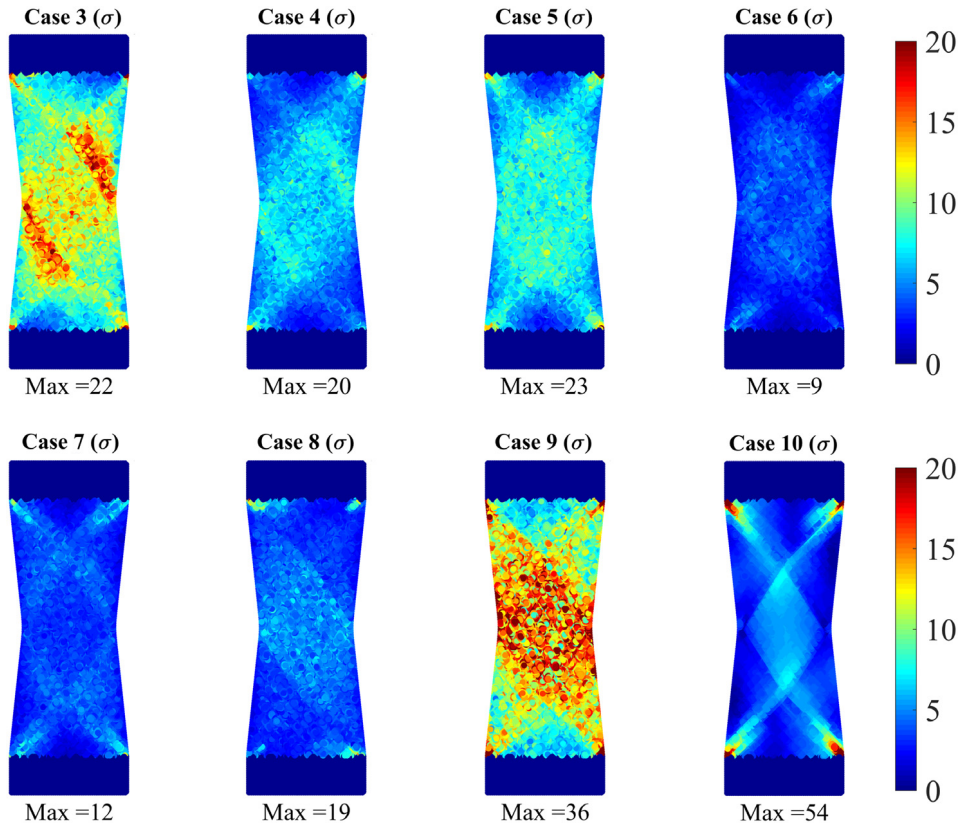

Fig. 16. (Color online) Effect of spatial variations on von-Mises stress field over the woven macroscopic composite: For cases 3 through 10, the fields are averaged over the 30 simulations. All fields have the same color bar where the maximum is set to 500 MPa for better comparison. The maximum stress is provided below each field.

Fig. 17. (Color online) Effect of random spatial variations on von-Mises stress field over the woven macroscopic composite: The fields quantify the standard deviation of the stress field over the 30 simulations. All fields have the same color bar where the maximum is set to 20 MPa for better comparison. The maximum standard deviation is provided below each field.

(such as metamodeling and sensitivity analyses) to address the computational costs. Our choice of random field enables manageable uncertainty quantification by directly relating the hyperparameters of the MRGP to the physical uncertainty sources. It also allows to couple the uncertainty sources across the spatial scales and build nested random fields that can model non-stationary and C^0 (i.e., continuous but not differentiable) fields at the fine-scale. These nested random fields are built through the top-down sampling scheme where the hyperparameters of MRGP models at the mesoscale are determined at the macroscale via a single (and separate) MRGP model.

We applied our approach to quantify the macroscale uncertainty in the linear analysis of a woven composite due to spatial variations of yarn angle, fiber volume fraction, and fiber misalignment angle. We chose such materials because they possess a hierarchical structure and are ubiquitously employed in aerospace, construction, and transportation industries. Computational homogenization technique was used to conduct the multiscale simulations where a monoclinic material model was employed to allow for modeling non-orthogonal woven RVE samples which exhibit different behavior spatially. We also modeled fiber misalignment in mesoscale cured woven RVE analyses by implementing a micro-plane triad model. Our results indicate that the effect of uncertainty sources on the materials' response at the macroscale, especially the stress field, could be significant. In particular, it was demonstrated that the spatial variations of the yarn angle have a considerable effect on both homogenized and local behavior in linear analyses of woven composites. The spatial variations of fiber volume fraction and misalignment angles have, relative to the yarn angle, negligible effect for the studied linear behavior. To the best of our knowledge, these effects have not been previously studied elsewhere.

Our microscale and mesoscale RVEs were sufficiently large and so more uncertainty would have been observed in the response had we chosen smaller RVEs. Additionally, we focused on the first and second moments of the response (i.e., the stress field) for macroscale uncertainty quantification. Higher moments should clearly be considered
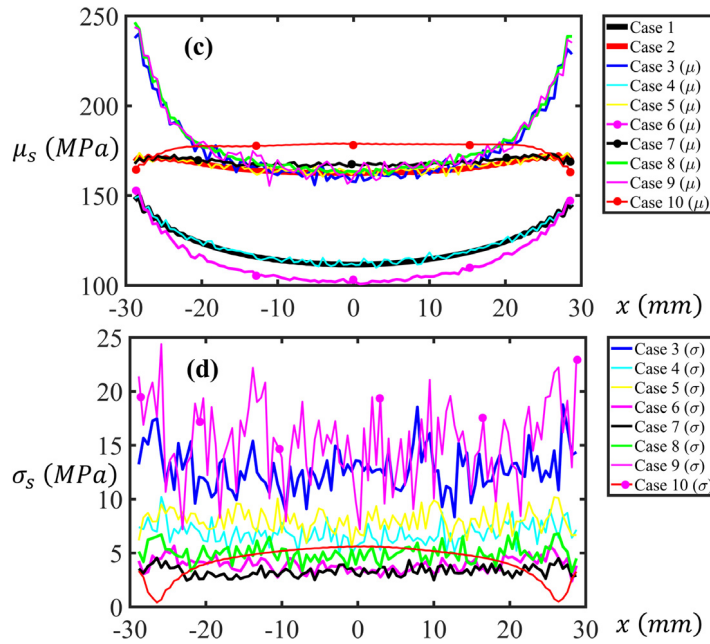
Fig. 18. (Color online) Von-Mises stress on the mid-section of the part: (a) The mean and (b) the standard deviation of stress at the mid-section. In cases 3 through 10, the mean and standard deviation are calculated for the 30 simulations.

to quantify the uncertainty more rigorously. Our choice on MRGPs implies a normality assumption which might not hold in other applications where the distributions are heavily skewed or appropriate transformations are not readily available. In such cases, other random field representations (see Section 2.1) can be integrated with the top-down sampling approach at the expense of more computations. We plan to gather experimental images from various structures at different spatial scales to further demonstrate the applications of our approach.

Acknowledgment

Appendix

A.1. Gaussian processes

Below, we first briefly describe the Gaussian process (GP) modeling procedure, i.e., how to estimate the parameters of a GP model given some training dataset (see [77,80,100] for more details). Then, we elaborate on how a learned GP model (or one whose parameters are known) can be used.

A.1.1. Parameter estimation in GP modeling

Let $x = [x_1, x_2, \ldots, x_d]^T$ and $y(x)$ denote, respectively, the set of input variables over the d-dimensional input space $\mathbb{R}^d$ and the scalar response function. Suppose we observe the q-dimensional response $y = [y_1(x_1), y_1(x_2), \ldots, y_1(x_n), \ldots, y_q(x_1), \ldots, y_q(x_n)]^T$ at n distinct locations $D = \{x_1, x_2, \ldots, x_n\}$ and wish to predict $y(x_0) = [y_1(x_0), \ldots, y_q(x_0)]^T$ for any $x_0 \epsilon \mathbb{R}^d$. The basic idea here is to model $y(x)$ as a realization of a GP, denoted by $Y(x)$, with the parametric mean and covariance function of:

$$E[Y(x)] = \beta, \tag{A.1}$$

$$c(x, x') = Cov[Y(x), Y(x')]. \tag{A.2}$$

As in this work we use the GP model for interpolation, reversion to the mean [101] is of no concern. Hence, we have prescribed a constant mean for the GP model but note that known basis functions (that depend on x) can also be employed. As for the covariance function, the most common choice is the so-called Gaussian covariance function (see Eq. (3.2)). The heart of GP modeling lies in estimating its hyperparameters (via training dataset) or adjusting them (based on prior knowledge or expertise). While for metamodeling (Section 4.5 these hyperparameters were estimated, in Sections 4.3 and 4.4 they were adjusted.

The hyperparameters of a GP model are denoted by β, Σ, and ω (see Eqs. (4.6) and (A.1)) which can be estimated via either the maximum likelihood estimation (MLE) or cross-validation (CV) methods. In this work, we use the MLE method as it is shown to be more robust and efficient [80]. Within the MLE framework, the hyperparameters are estimated by maximizing the multivariate Gaussian likelihood function:

$$
\begin{aligned}
\left[\hat{\beta}, \hat{\Sigma}, \hat{\omega}\right] &= \underset{\beta,\Sigma,\omega}{\operatorname{argmax}} \mathcal{L}\left[\beta, \Sigma, \omega | y\right] = \underset{\beta,\Sigma,\omega}{\operatorname{argmax}} \det\left(2\pi\left(\Sigma \bigotimes R\right)\right)^{-\frac{1}{2}} \exp\left\{-\frac{1}{2}\left(y\right.\right.\\
&\left.\left. - 1 \bigotimes \beta\right)^T \left(\Sigma \bigotimes R\right)^{-1}\left(y - 1 \bigotimes \beta\right)\right\},
\end{aligned}
\tag{A.3}
$$

where $\log\left(\cdot\right)$ is the natural logarithm and R is an $n \times n$ matrix with (i, j)th element $R_{ij} = r\left(x_i, x_j\right)$ for $i, j = 1, \ldots, n$. Once the hyperparameters are estimated, the GP predictor for $y(x_0)$ and its associated mean squared error (MSE) can be calculated with:

$$
\hat{y}\left(x_0\right) = \hat{\beta} + r'^T\left(x_0\right) R^{-1}(y - 1\bigotimes \hat{\beta}),
\tag{A.4}
$$

$$
MSE\left[\hat{y}\left(x_0\right)\right] = \Sigma \bigotimes \left(r\left(x_0, x_0\right) - r'^T\left(x_0\right) R^{-1} r'\left(x_0\right) + W^T\left(1^T R^{-1} 1\right)^{-1} W\right),
\tag{A.5}
$$

where $W = 1 - 1^T R^{-1} r\left(x_0\right)$ and $r\left(x_0\right)$ is an $n \times 1$ vector whose ith element is $r\left(x_i, x_0\right)$.

A.1.2. Using a GP model

Given the mean and covariance matrix of a GP model in Eqs. (A.4) and (A.5), one can draw a random realization from the GP model using the multi-variate Gaussian distribution. For instance, this can be achieved via the *mvnrnd()* function in MATLAB. We note that, if the GP model is learned using a dataset (e.g., for metamodeling purposes), the hyperparameters are estimated (e.g., via MLE). Otherwise, the user defines the hyperparameters but must make sure that the defined covariance matrix is positive definite (as we have done in Sections 4.3 and 4.4).

A.2. Details on the sensitivity studies at the mesoscale

In Section 4.4 it was illustrated that only the average values of fiber volume fraction and zenith angle (one component of the misalignment angle) affected the homogenized response of a woven RVE at the mesoscale. These two parameters are controlled by the corresponding mean values of the MRGP that models the mesoscale spatial variations (i.e., β_v and β_θ). The other parameters of the MRGP model (i.e., β_φ, σ_{vv}^2, $\sigma_{\varphi\varphi}^2$, $\sigma_{\theta\theta}^2$, $\sigma_{v\varphi}^2$, $\sigma_{v\theta}^2$, $\sigma_{\varphi\theta}^2$, ω_x, ω_y, and ω_z) were found to affect the homogenized response insignificantly through sensitivity studies.

In our sensitivity studies, we investigated the uncertainty sources one by one. That is, all the hyperparameters of the MRGP model were fixed except for those controlling one uncertainty source. For instance, to investigate the effect of fiber volume fraction and its spatial variations, β_v and σ_{vv}^2 were changed while the rest of the MRGP hyperparameters were fixed. For each combination of β_v and σ_{vv}^2, then, 30 independent samples were generated from the MRGP model to account for the inherent randomness. Next, the variability of the effective moduli of the woven RVE among these simulations was quantified. If the variability was significant, the parameter was deemed as important. Otherwise, it was set as a constant and, subsequently, not considered in the metamodeling stage in Section 4.5 (because it would not change in the multiscale simulations). Below, we demonstrate one of the cases where the significance of local fiber volume fraction is investigated.

The average value and spatial variations of v are controlled via β_v and σ_v^2, respectively. Hence, we fixed the other parameters and took 30 random and independent realizations from the mesoscale MRGP model for each combination of β_v and σ_v^2. The considered values for β_v and σ_v^2 are, respectively, [45, 50, 55, 60, 65] % and [9, 16] %. In this case, the rest of the hyperparameters (i.e., β_θ, β_φ, $\sigma_{\varphi\varphi}^2$, $\sigma_{\theta\theta}^2$, $\sigma_{v\varphi}^2$, $\sigma_{v\theta}^2$, $\sigma_{\varphi\theta}^2$) were set to zero to have the variability be only a function of spatial variations on v. Fig. 19 summarizes the results of 30 mesoscale simulations where $\beta_v = 65\%$
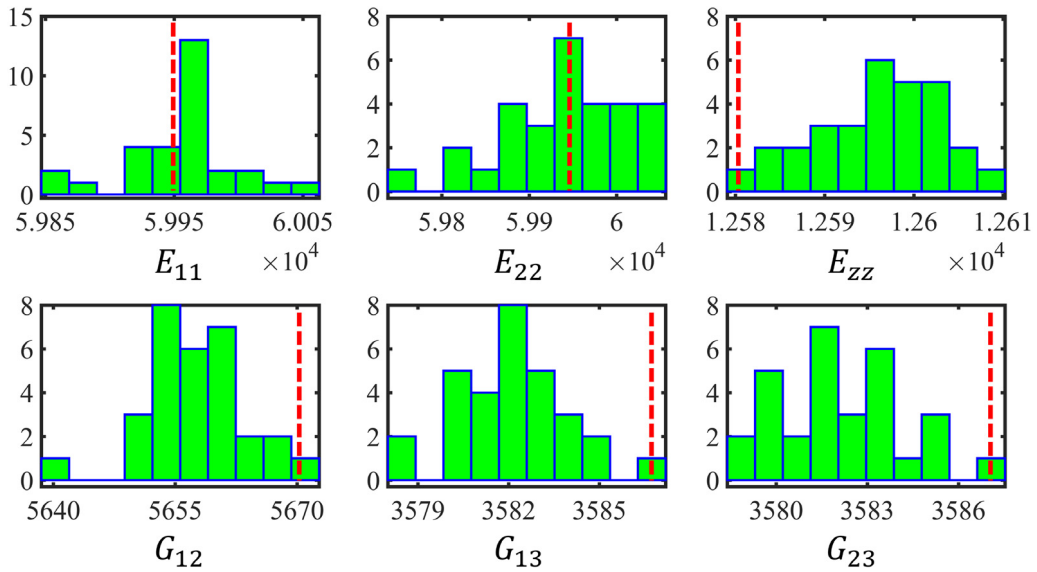
Fig. 19. Variation of moduli (MPa) in a woven RVE due to spatial variations of fiber volume fraction (v): The effective moduli change due to the variations in the local fiber volume fraction. The changes are, however, insignificant. Herein, $\beta_v = 65\%$ and $\sigma_{vv}^2 = 16\%$. Since the latter parameters is nonzero, 30 simulations were conducted to quantify the effect of variations. The dashed red lines correspond to the moduli when $\sigma_{vv}^2 = 0$.

and $\sigma_v^2 = 16\%$. The dashed red line corresponds to the moduli of a woven RVE with $\sigma_v^2 = 0\%$ (i.e., with no spatial variations). As it can be observed, the spatial variations do not significantly affect the homogenized response of a woven RVE and hence, one can only consider the average fiber volume fraction. Such analyses were conducted for various combinations and the results are summarized in Fig. 11 for the three parameters v, θ, and φ. In the cases where θ and φ changed, the simulated annealing algorithm was used to ensure that $\sum_{i=1}^{N} \sin\left(\theta_i^2\right) \cos\left(\varphi_i^2\right) = 0$ and $\sum_{i=1}^{N} \sin\left(\theta_i^2\right) \sin\left(\varphi_i^2\right) = 0$ at each yarn cross-section to avoid changing the yarn angle due to fiber misalignment (N denotes the number of IPs on the yarn cross-section).

A.3. Conditional distribution

If $X = [X_1, \ldots, X_n]^T$ and $Y = [Y_1, \ldots, Y_m]^T$ are jointly Gaussian:

$$\begin{bmatrix} Y \\ X \end{bmatrix} \sim \mathbb{N}_{m+n}\left(\begin{bmatrix} \mu_Y \\ \mu_X \end{bmatrix}, \begin{bmatrix} \Sigma_{YY} & \Sigma_{YX} \\ \Sigma_{XY} & \Sigma_{XX} \end{bmatrix} \right), \tag{A.6}$$

where $\mathbb{N}_{m+n}$ denotes the multivariate normal distribution, $\mu_Y = E[Y]$, $\mu_X = E[X]$, $\Sigma_{YY} = Cov(Y, Y)$, $\Sigma_{XX} = Cov(X, X)$, $\Sigma_{YX} = \Sigma_{XY}^T = Cov(Y, X) = E\left[(X - \mu_X)(Y - \mu_Y)^T\right]$, and $E[\cdot]$ denotes the expectation operator. The conditional distribution of Y given X is:

$$Y|X \sim \mathbb{N}_m\left(\mu_Y + \Sigma_{YX}\Sigma_{XX}^{-1}(X - \mu_X), \Sigma_{YY} - \Sigma_{YX}\Sigma_{XX}^{-1}\Sigma_{YX}^T\right). \tag{A.7}$$

In our example, $Y = [v, \theta]$ and $X = \alpha$.

References

[1] S. Rahimi-Aghdam, Z.P. Bažant, F.C. Caner, Diffusion-controlled and creep-mitigated ASR damage via microplane model. II: Material degradation, drying, and verification, J. Eng. Mech. 143 (2) (2017).

[2] Z.P. Bažant, S. Rahimi-Aghdam, Diffusion-controlled and creep-mitigated ASR damage via microplane model. I: Mass concrete, J. Eng. Mech. 143 (2) (2017).

[3] R. Rezakhani, G. Cusatis, Asymptotic expansion homogenization of discrete fine-scale models with rotational degrees of freedom for the simulation of quasi-brittle materials, J. Mech. Phys. Solids 88 (2016) 320–345.

[4] R. Rezakhani, X.W. Zhou, G. Cusatis, Adaptive multiscale homogenization of the lattice discrete particle model for the analysis of damage and fracture in concrete, Int. J. Solids Struct. 125 (2017) 50–67.

[5] K. Matouš, et al., A review of predictive nonlinear theories for multiscale modeling of heterogeneous materials, J. Comput. Phys. 330 (2017) 192–220.

[6] A. Chernatynskiy, S.R. Phillpot, R. LeSar, Uncertainty quantification in multiscale simulation of materials: a prospective, Annu. Rev. Mater. Res. 43 (1) (2013) 157–182.

[7] W.K. Liu, et al., Complexity science of multiscale materials via stochastic computations, Internat. J. Numer. Methods Engrg. 80 (6–7) (2009) 932–978.

[8] D.W. Apley, J. Liu, W. Chen, Understanding the effects of model uncertainty in robust design with computer experiments, J. Mech. Des. 128 (4) (2006) 945–958.

[9] M.A. Bessa, et al., A framework for data-driven analysis of materials under uncertainty: Countering the curse of dimensionality, Comput. Methods Appl. Mech. Engrg. 320 (2017) 633–667.

[10] M.S. Greene, et al., Computational uncertainty analysis in multiresolution materials via stochastic constitutive theory, Comput. Methods Appl. Mech. Engrg. 200 (1–4) (2011) 309–325.

[11] M.S. Greene, et al., A generalized uncertainty propagation criterion from benchmark studies of microstructured material systems, Comput. Methods Appl. Mech. Engrg. 254 (2013) 271–291.

[12] A.B. Ilyani Akmar, et al., Uncertainty quantification of dry woven fabrics: A sensitivity analysis on material properties, Compos. Struct. 116 (2014) 1–17.

[13] B. Kouchmeshky, N. Zabaras, Microstructure model reduction and uncertainty quantification in multiscale deformation processes, Comput. Mater. Sci. 48 (2) (2010) 213–227.

[14] J. McFarland, et al., Calibration and uncertainty analysis for computer simulations with multivariate output, AIAA J. 46 (5) (2008) 1253–1265.

[15] S. Reeve, A. Strachan, Error correction in multi-fidelity molecular dynamics simulations using functional uncertainty quantification. 2016. arXiv preprint arXiv:1603.00599.

[16] P. Sasikumar, R. Suresh, S. Gupta, Stochastic model order reduction in uncertainty quantification of composite structures, Compos. Struct. 128 (2015) 21–34.

[17] D. Savvas, G. Stefanou, Assessment of the effect of microstructural uncertainty on the macroscopic properties of random composite materials, J. Compos. Mater. (2016) 0021998316677333.

[18] S. Sriramula, M.K. Chryssanthopoulos, Quantification of uncertainty modelling in stochastic analysis of FRP composites, Composites A 40 (11) (2009) 1673–1684.

[19] D.A. Stainforth, et al., Uncertainty in predictions of the climate response to rising levels of greenhouse gases, Nature 433 (7024) (2005) 403–406.

[20] J. Zhang, M.D. Shields, On the quantification and efficient propagation of imprecise probabilities resulting from small datasets, Mech. Syst. Signal Process. 98 (2018) 465–483.

[21] R. Bostanabad, et al., Stochastic microstructure characterization and reconstruction via supervised learning, Acta Mater. 103 (2016) 89–102.

[22] R. Bostanabad, W. Chen, D.W. Apley, Characterization and reconstruction of 3D stochastic microstructures via supervised learning, J. Microsc. 264 (3) (2016) 282–297.

[23] R. Bostanabad, et al., Computational microstructure characterization and reconstruction: Review of the state-of-the-art techniques, Prog. Mater. Sci. 95 (2018) 1–41.

[24] M. Komeili, A. Milani, The effect of meso-level uncertainties on the mechanical response of woven fabric composites under axial loading, Comput. Struct. 90 (2012) 163–171.

[25] A. Tabiei, W. Yi, Comparative study of predictive methods for woven fabric composite elastic properties, Compos. Struct. 58 (1) (2002) 149–164.

[26] A. Tabiei, I. Ivanov, Fiber reorientation in laminated and woven composites for finite element simulations, J. Thermoplast. Compos. Mater. 16 (5) (2003) 457–474.

[27] A. Vanaerschot, et al., Variability in composite materials properties, in: Applied Mechanics and Materials, Trans Tech Publ, 2015.

[28] G. Requena, et al., 3D-Quantification of the distribution of continuous fibres in unidirectionally reinforced composites, Composites A 40 (2) (2009) 152–163.

[29] Y. Mahadik, S. Hallett, Effect of fabric compaction and yarn waviness on 3D woven composite compressive properties, Composites A 42 (11) (2011) 1592–1600.

[30] H. Lin, et al., Automated geometric modelling of textile structures, Text. Res. J. 82 (16) (2012) 1689–1702.

[31] R. Zulkifli, et al., Interlaminar fracture toughness of multi-layer woven silk/epoxy composites treated with coupling agent, Eur. J. Sci. Res. 27 (3) (2009) 454–462.

[32] F. Feyel, J.-L. Chaboche, FE 2 multiscale approach for modelling the elastoviscoplastic behaviour of long fibre SiC/Ti composite materials, Comput. Methods Appl. Mech. Engrg. 183 (3) (2000) 309–330.

[33] F. Feyel, A multilevel finite element method (FE 2) to describe the response of highly non-linear structures using generalized continua, Comput. Methods Appl. Mech. Engrg. 192 (28) (2003) 3233–3244.

[34] Z. Liu, M. Bessa, W.K. Liu, Self-consistent clustering analysis: an efficient multi-scale scheme for inelastic heterogeneous materials, Comput. Methods Appl. Mech. Engrg. 306 (2016) 319–341.

[35] Z. Liu, M. Fleming, W.K. Liu, Microstructural material database for self-consistent clustering analysis of elastoplastic strain softening materials, Comput. Methods Appl. Mech. Engrg. 330 (2018) 547–577.

[36] Z. Liu, et al., Data-driven self-consistent clustering analysis of heterogeneous materials with crystal plasticity, in: Advances in Computational Plasticity, Springer, 2018, pp. 221–242.

[37] S. Tang, L. Zhang, W.K. Liu, From virtual clustering analysis to self-consistent clustering analysis: a mathematical study, Comput. Mech. (2018) 1–18.

[38] A. Vanaerschot, et al., Identification and quantification of variability in woven composite materials based on carbon fibre weaves. 2015.

[39] T.W. Simpson, D.K. Lin, W. Chen, Sampling strategies for computer experiments: design and analysis, Int. J. Reliab. Appl. 2 (3) (2001) 209–240.

[40] R. Jin, W. Chen, A. Sudjianto, An efficient algorithm for constructing optimal design of computer experiments, J. Statist. Plann. Inference 134 (1) (2005) 268–287.

[41] M.D. Shields, J. Zhang, The generalization of Latin hypercube sampling, Reliab. Eng. Syst. Saf. 148 (2016) 96–108.

[42] M. Chiachio, J. Chiachio, G. Rus, Reliability in composites–A selective review and survey of current development, Composites B 43 (3) (2012) 902–913.

[43] D. Savvas, et al., Effect of waviness and orientation of carbon nanotubes on random apparent material properties and RVE size of CNT reinforced composites, Compos. Struct. 152 (2016) 870–882.

[44] D. Savvas, G. Stefanou, M. Papadrakakis, Determination of RVE size for random composites with local volume fraction variation, Comput. Methods Appl. Mech. Engrg. 305 (2016) 340–358.

[45] H. Hsiao, I. Daniel, Effect of fiber waviness on the high-strain-rate behavior of composites, J. Thermoplast. Compos. Mater. 12 (5) (1999) 412–422.

[46] H. Hsiao, I. Daniel, Nonlinear elastic behavior of unidirectional composites with fiber waviness under compressive loading, J. Eng. Mater. Technol. 118 (4) (1996) 561–570.

[47] H. Hsiao, I. Daniel, Effect of fiber waviness on stiffness and strength reduction of unidirectional composites under compressive loading, Compos. Sci. Technol. 56 (5) (1996) 581–593.

[48] R.G. Gallager, Stochastic Processes: Theory for Applications, Cambridge University Press, 2013.

[49] M. Grigoriu, On the spectral representation method in simulation, Probab. Eng. Mech. 8 (2) (1993) 75–90.

[50] Z. Jiang, W. Chen, C. Burkhart, Efficient 3D porous microstructure reconstruction via Gaussian random field and hybrid optimization, J. Microsc. 252 (2) (2013) 135–148.

[51] J.A. Quiblier, A new three-dimensional modeling technique for studying porous media, J. Colloid Interface Sci. 98 (1) (1984) 84–102.

[52] J.W. Cahn, Phase separation by spinodal decomposition in isotropic systems, J. Chem. Phys. 42 (1) (1965) 93–+.

[53] S.C. Yu, et al., Characterization and design of functional quasi-random nanostructured materials using spectral density function, in: Proceedings of the Asme International Design Engineering Technical Conferences and Computers and Information in Engineering Conference, Vol. 2b, 2016, pp. 135–145.

[54] G. Deodatis, R.C. Micaletti, Simulation of highly skewed non-Gaussian stochastic processes, J. Eng. Mech. 127 (12) (2001) 1284–1295.

[55] N.D. Lagaros, G. Stefanou, M. Papadrakakis, An enhanced hybrid method for the simulation of highly skewed non-Gaussian stochastic fields, Comput. Methods Appl. Mech. Engrg. 194 (45) (2005) 4824–4844.

[56] R. Popescu, G. Deodatis, J.H. Prevost, Simulation of homogeneous nonGaussian stochastic vector fields, Probab. Eng. Mech. 13 (1) (1998) 1–13.

[57] M. Grigoriu, Applied Non-Gaussian Processes: Examples, Theory, Simulation, Linear Random Vibration, and MATLAB Solutions, Prentice Hall, 1995.

[58] F. Lindskog, Modelling Dependence with Copulas and Applications to Risk Management (Master Thesis), ETH Zürich, 2000.

[59] E.W. Frees, P. Wang, Credibility using copulas, N. Am. Actuar. J. 9 (2) (2005) 31–48.

[60] J.V. Rosenberg, T. Schuermann, A general approach to integrated risk management with skewed, fat-tailed risks, J. Financ. Econ. 79 (3) (2006) 569–614.

[61] Y. Noh, K. Choi, L. Du, Reliability-based design optimization of problems with correlated input variables using a Gaussian Copula, Struct. Multidiscip. Optim. 38 (1) (2009) 1–16.

[62] C. Genest, A.-C. Favre, Everything you always wanted to know about copula modeling but were afraid to ask, J. Hydrol. Eng. 12 (4) (2007) 347–368.

[63] R.G. Ghanem, P.D. Spanos, Stochastic Finite Elements: A Spectral Approach, Courier Corporation, 2003.

[64] G. Stefanou, The stochastic finite element method: Past, present and future, Comput. Methods Appl. Mech. Engrg. 198 (9) (2009) 1031–1051.

[65] G. Stefanou, D. Savvas, M. Papadrakakis, Stochastic finite element analysis of composite structures based on material microstructure, Compos. Struct. 132 (2015) 384–392.

[66] X.F. Xu, A multiscale stochastic finite element method on elliptic problems involving uncertainties, Comput. Methods Appl. Mech. Engrg. 196 (25) (2007) 2723–2736.

[67] D. Xiu, G.E. Karniadakis, Modeling uncertainty in steady state diffusion problems via generalized polynomial chaos, Comput. Methods Appl. Mech. Engrg. 191 (43) (2002) 4927–4948.

[68] W.K. Liu, T. Belytschko, A. Mani, Random field finite elements, Internat. J. Numer. Methods Engrg. 23 (10) (1986) 1831–1845.

[69] A. Der Kiureghian, J.-B. Ke, The stochastic finite element method in structural reliability, in: Stochastic Structural Mechanics, Springer, 1987, pp. 84–109.

[70] G. Deodatis, Weighted integral method. I: stochastic stiffness matrix, J. Eng. Mech. 117 (8) (1991) 1851–1864.

[71] E. Vanmarcke, M. Grigoriu, Stochastic finite element analysis of simple beams, J. Eng. Mech. 109 (5) (1983) 1203–1214.

[72] P.D. Spanos, R. Ghanem, Stochastic finite element expansion for random media, J. Eng. Mech. 115 (5) (1989) 1035–1053.

[73] J. Argyris, M. Papadrakakis, G. Stefanou, Stochastic finite element analysis of shells, Comput. Methods Appl. Mech. Engrg. 191 (41) (2002) 4781–4804.

[74] G. Falsone, G. Ferro, An exact solution for the static and dynamic analysis of FE discretized uncertain structures, Comput. Methods Appl. Mech. Engrg. 196 (21) (2007) 2390–2400.

[75] B. Van den Nieuwenhof, J.-P. Coyette, Modal approaches for the stochastic finite element analysis of structures with material and geometric uncertainties, Comput. Methods Appl. Mech. Engrg. 192 (33) (2003) 3705–3729.

[76] I. Hassaninia, et al., Characterization of the optical properties of turbid media by supervised learning of scattering patterns, Sci. Rep. 7 (1) (2017) 15259.

[77] J. Sacks, et al., Design and analysis of computer experiments, Statist. Sci. (1989) 409–423.

[78] M.C. Kennedy, A. O'Hagan, Predicting the output from a complex computer code when fast approximations are available, Biometrika 87 (1) (2000) 1–13.

[79] T.W. Simpson, et al., Metamodels for computer-based engineering design: survey and recommendations, Eng. Comput. 17 (2) (2001) 129–150.

[80] J.D. Martin, T.W. Simpson, Use of kriging models to approximate deterministic computer models, AIAA J. 43 (4) (2005) 853–863.

[81] M. Plumlee, D.W. Apley, Lifted Brownian kriging models, Technometrics (2016) (just-accepted).

[82] S. Tao, et al., Enhanced gaussian process metamodeling and collaborative optimization for vehicle suspension design optimization, in: ASME 2017 International Design Engineering Technical Conferences and Computers and Information in Engineering Conference, American Society of Mechanical Engineers, 2017.

[83] R. Bostanabad, et al., Leveraging the nugget parameter for efficient Gaussian process modeling, Internat. J. Numer. Methods Engrg. (2018) n/a–n/a.

[84] C.E. Rasmussen, Gaussian processes for machine learning. 2006.

[85] H.Y. Xu, et al., A descriptor-based design methodology for developing heterogeneous microstructural materials system, J. Mech. Des. 136 (5) (2014) 051007.

[86] J. Snoek, H. Larochelle, R.P. Adams, Practical bayesian optimization of machine learning algorithms, in: Advances in Neural Information Processing Systems, 2012.

[87] M.C. Kennedy, A. O'Hagan, Bayesian calibration of computer models, J. R. Stat. Soc. Ser. B Stat. Methodol. 63 (3) (2001) 425–464.

[88] P.D. Arendt, D.W. Apley, W. Chen, Quantification of model uncertainty: Calibration, model discrepancy, and identifiability, J. Mech. Des. 134 (10) (2012) 100908.

[89] P.D. Arendt, et al., Improving identifiability in model calibration using multiple responses, J. Mech. Des. 134 (10) (2012) 100909.

[90] M.J. Bayarri, et al., A framework for validation of computer models, Technometrics (2012).

[91] P.D. Arendt, D.W. Apley, W. Chen, A preposterior analysis to predict identifiability in the experimental calibration of computer models, IIE Trans. 48 (1) (2016) 75–88.

[92] S. Green, et al., Mechanical modelling of 3D woven composites considering realistic unit cell geometry, Compos. Struct. 118 (2014) 284–293.

[93] X. Peng, J. Cao, A dual homogenization and finite element approach for material characterization of textile composites, Composites B 33 (1) (2002) 45–56.

[94] H. Huang, A.M. Waas, Compressive response of Z-pinned woven glass fiber textile composite laminates: Modeling and computations, Compos. Sci. Technol. 69 (14) (2009) 2338–2344.

[95] W. Zhang, et al., A non-orthogonal material model of woven composites in the preforming process, CIRP Ann-Manuf. Technol. (2017).

[96] A. Melro, et al., Micromechanical analysis of polymer composites reinforced by unidirectional fibres: Part II–micromechanical analyses, Int. J. Solids Struct. 50 (11) (2013) 1906–1915.

[97] K. Kirane, M. Salviato, Z.P. Bažant, Microplane triad model for simple and accurate prediction of orthotropic elastic constants of woven fabric composites, J. Compos. Mater. 50 (9) (2016) 1247–1260.

[98] I.M. Sobol, On quasi-Monte Carlo integrations, Math. Comput. Simulation 47 (2–5) (1988) 103–112.

[99] I.Y.M. Sobol', On the distribution of points in a cube and the approximate evaluation of integrals, Zh. Vychisl. Mat. Mat. Fiz. 7 (4) (1967) 784–802.

[100] N. Cressie, The origins of kriging, Math. Geol. 22 (3) (1990) 239–252.

[101] V.R. Joseph, Limit kriging, Technometrics 48 (4) (2006) 458–466.